Exploring the edge

Contigiani, O.

Chapter 6

Learning how to surf: studies in gravitational-wave cosmology

We investigate the relationship between the large-scale structure of the Universe and the gravitational wave (GW) signals emitted by merging binaries of astrophysical origin. We first study the effects of gravitational lensing on the observed population. By making minimal assumptions about the distribution of intrinsic properties, we show that lensing effects leave a recognizable signature on the observed rates and that they are prominent mainly at low inferred redshifts. We then consider the spatial cross-correlation of galaxy catalogs with either an unresolved GW background or catalogs of resolved GW sources. The first signal can constrain the evolution of the emitting population over cosmic time, while the second can be used to constrain the propagation of tensor metric perturbations. Our results suggest that galaxy surveys and GW signals will be powerful probes for both the astrophysical properties of the merging population and cosmology. Using mock data based on a simplified model, we show how our predictions can be re-scaled to multiple instrumental configurations. We find that a higher spatial resolution improves constraints across the board, but accurate distance measurements are essential for cosmological applications.

Omar Contigiani
2020, Monthly Notices of the Royal Astronomical Society, 492, 3359

Guadalupe Cañas-Herrera, Omar Contigiani, and Valeri Vardanyan
2021, The Astrophysical Journal, 918, 20
2020, Physical Review D, 102, 043513

6.1 Introduction

Gravitational waves (GWs) are one of the most striking predictions of the General Theory of Relativity (Einstein, 1916, 1918) and their direct detection by the LIGO-Virgo collaboration (Abbott et al., 2016) triggered a rapidly increasing interest in exploiting this new field for cosmological information. In this chapter, we summarize three works pushing toward this objective.

In Section 6.2 we discuss the consequences of gravitational magnification, i.e., the enlargement of a source in the image plane of an observer due to the converging effect of one or more gravitational lenses along the line of sight. For point-like EM sources, this corresponds to an increase in brightness by a factor μ, which has been shown to affect the bright end of the luminosity functions of high redshift quasars and submillimeter galaxies (e.g. Negrello et al., 2010; Wyithe and Loeb, 2002). Similarly, the effects of magnification on the GW signals emitted by merging binary compact objects introduces a long and highly suppressed tail in the observed distribution (e.g. Dai et al., 2017; Oguri, 2018; Smith et al., 2018). Recently, Broadhurst et al. (2018) claimed that a considerable fraction of LIGO-Virgo events to date might belong to this tail and that another sign of strong lensing, i.e., multiple images originating from the same source, might have already been detected (Broadhurst et al., 2019). While this idea explains the present-day tension with binary evolution models (see e.g. Dominik et al., 2012) that predict lower masses than what is observed, the hypothesis is not favored by the data (Hannuksela et al., 2019; Singer et al., 2019). Furthermore, the tension it tries to explain might also be alleviated through tweaks to stellar evolution models (Abbott et al., 2016). The goal of Section 6.2 is to offer general quantitative insights into the effects of lensing on the expected rates of gravitational wave mergers and call attention to its general low likelihood in light of the aforementioned claims.[1]

GWs alone are not particularly useful for general cosmological applications because near future data will only provide rough estimates of the sky position and luminosity distance to the source. However, they can serve as powerful cosmological probes when combined with electromagnetic (EM) data, from which redshifts can be extracted. This idea dates back to Schutz (1986), and in Section 6.3 and 6.4, we discuss in detail how one can exploit the spatial correlation between the galaxies hosting GW events and the galaxies observed by wide surveys for cosmological applications.

First, we study the cross-correlation signal between an unresolved GW background (GWB) and galaxy catalogs, arguing why it represents the ideal observable to detect and measure said background. In the past, the anisotropies of the astrophysical GWB have been extensively studied (Thrane et al., 2009) and, more recently, two independent groups *Cusin et. al.* (Cusin et al., 2018, 2017) and *Jenkins et. al.* (Jenkins, Alexander C. and Sakellariadou, Mairi, 2018; Jenkins et al., 2018) obtained discrepant predictions for

[1] In the interest of reproducibility, a Jupyter notebook offering a guided version of this section is available at https://www.github.com/contigiani/lensingGW.

the scale-dependent signal (Cusin et al., 2018; Jenkins et al., 2019b). The main disagreements are related to the shape of the angular power spectrum as well as the overall amplitude of the signal. In this work, we explain how the difference in shape is related to the treatment of non-linear scales (see Section 6.3.1), whereas the difference in amplitude is simply due to the chosen normalization. Apart from this necessary clarification, we focus almost exclusively on the cross-correlation of the GWB with galaxies and quantify its constraining power. We choose to work with this observable for two main reasons. (1) the cross-correlation signal for diffuse backgrounds is expected to have a larger signal-to-noise ratio compared to the autocorrelation signal and is likely to be detected earlier (Ando et al., 2014), (2) the autocorrelation signal of the astrophysical GWB is susceptible to small scales and nearby structures, while the cross-correlation signal GW is free from this problem.

Second, in Section 6.4, we explore ways to reconstruct the difference between models of modified gravity and GR using resolved GW sources in combination with galaxy catalogs. An altered friction term for GWs arises in extended models displaying a redshift-dependent gravitational coupling (Amendola et al., 2018; Belgacem et al., 2018) and, as a result, the inferred luminosity distance to GW sources differs from the corresponding EM luminosity distance. It should be noted that this interesting phenomenon can already be loosely constrained today using multiple techniques, e.g. using the multimessenger detection of GW170817 (Arai and Nishizawa, 2018; Lagos et al., 2019) or features in the mass distribution of existing GW catalogs (María Ezquiaga, 2021). In addition to presenting our formalism, we also show how to jointly reconstruct the redshift evolution of modified gravity effects and the bias of GW sources. The reconstruction method we make use of is based on Gaussian processes (GPs), a well-known hyperparametric regression procedure (Rasmussen and Williams, 2005).

Unless stated otherwise, our fiducial cosmology is based on the best fit results from Planck 2018 (Aghanim et al., 2020). In our analysis, we use COLOSSUS (Diemer, 2018) and `Astropy` (Robitaille et al., 2013; Price-Whelan et al., 2018) for cosmological calculations, `sklearn` (Scikit-learn, 2018) for the GP implementation, `emcee` (Foreman-Mackey et al., 2013) as our posterior sampler and `GetDist` (Lewis, 2019) to plot the final contours.

6.2 Lensing boost

6.2.1 Formalism

The value of the magnification μ for cosmological sources at various redshifts z is modeled by a probability function $P(\mu, z)$ which can be obtained numerically by performing ray-tracing simulations (e.g. Hilbert et al., 2007; Takahashi et al., 2011). To simplify the notation, here we call $P(\mu)$ what is sometimes called $\frac{dP}{d\mu}$ in the literature. This quantity measures the distribution of magnification for all possible images of a given source and due to conservation of photons/gravitons on average we have null magnification,

$$\langle \mu \rangle = \int d\mu \; \mu P(\mu, z) = 1. \tag{6.1}$$

More details about how this distribution should be interpreted are available in appendix A of Oguri (2018).

For this section, we will use a simplified model of $P(\mu, z)$, calculated as the sum of two components: weak and strong lensing. For the first, we assume a log-normal distribution for the convergence κ (as in, e.g. Taruya et al., 2002; Hada and Futamase, 2018) and derive the corresponding magnification probability density function using the relation:

$$\mu \simeq \frac{1}{(1-\kappa)^2}. \tag{6.2}$$

While this relation for μ and κ is valid only in the limit of null shear $|\gamma| = 0$, it has been shown to accurately reproduce the weak lensing component of the magnification distribution (Takahashi et al., 2011), where $\kappa \lesssim 1$. For the strong-lensing component, we do not assume any relation between $\mu, \kappa, |\gamma|$ and instead impose a power-law $P(\mu, z) \propto \mu^{-3}$ for $\mu > 1$, calibrated empirically using the lensing depths of Oguri (2018). Finally, to simulate the demagnification tail, we assume a constant value for $\mu < 1$. We point out that we do not consider sources with $z > 10$ in this work.

For EM sources, the source flux is amplified by a factor μ in the presence of magnification. If the redshift to the source is known and a cosmology is assumed, the result is a mismatch between the inferred luminosity ($\mathcal{L}$) and the intrinsic one ($\mathcal{L}_*$):

$$\frac{\mathcal{L}}{\mathcal{L}_*} = \mu. \tag{6.3}$$

If only the luminosity is known, then the result is a mismatch between the inferred and actual luminosity distance to the source:

$$D(z) = \frac{D(z_*)}{\sqrt{\mu}}, \tag{6.4}$$

where we call z and z_* the inferred redshift and the true one, respectively. We also refer to the corresponding luminosity distances as D and D_*. This case applies to

Supernovae type IA (SNIa), a category of transient events known as standard candles because they share the same intrinsic luminosity. The Jacobians of the transformations in Eqs. (6.3) and (6.4) are:

$$\frac{\partial \mathcal{L}_*}{\partial \mathcal{L}} = \frac{1}{\mu}, \tag{6.5}$$

and

$$\frac{\partial z_*}{\partial z} = \frac{D'(z)}{D'(z_*)}\sqrt{\mu}. \tag{6.6}$$

In the case of GWs, we limit ourselves to the inspiral phase of compact binary mergers. In this phase, the gravitational wave strain amplitude as a function of time, $h(t)$, carries information about the source's distance and the associated masses. The frequency evolution of the signal can be used to extract the redshifted chirp mass (an effective combination of the masses involved in the merger):

$$\dot{f} \propto \mathcal{M}(1+z), \tag{6.7}$$

while the amplitude is connected to the inverse of the luminosity distance:

$$h(t) \propto \frac{A\left(\mathcal{M}(1+z)\right)}{D(z)}, \tag{6.8}$$

where $A(-)$ is a function of the redshifted chirp mass alone. From this, it should be clear that both $\mathcal{M}$ and $D(z)$ can be extracted from the signal.

In the presence of magnification, the observed strain is multiplied by a factor $\sqrt{\mu}$, and the mismatch between the intrinsic properties $(z_*, \mathcal{M}_*)$ and the inferred ones $(z, \mathcal{M})$ is such that

$$D(z) = \frac{D(z_*)}{\sqrt{\mu}}, \tag{6.9}$$

and

$$\mathcal{M} = \mathcal{M}_* \frac{1+z_*}{1+z}. \tag{6.10}$$

For $\mu > 1$ this implies that distant events are assumed to be closer and more massive than they actually are, just like magnified electromagnetic sources are assumed brighter. An essential difference between the two, however, is that the dependence on magnification is significantly weaker for the GW merger parameter $\mathcal{M}$ compared to the luminosity $\mathcal{L}$,

$$\frac{\mathcal{M}}{\mathcal{M}_*} = \frac{1+z_*}{1+z} \propto \mu^{s(z)}, \tag{6.11}$$

with $s(z) < 0.5$ for any $z < z_*$ and $s(z) \to 0.5$ for increasing z. This can be easily shown by combining Eq. (6.9) and (6.10), together with the fact that the luminosity distance can be expressed, in a flat background, as the product of $(1+z)$ and a strictly increasing function of z (comoving distance).

To conclude this section, it is useful to point out that the Jacobian of the transformation $(\mathcal{M}, z) \leftrightarrow (\mathcal{M}_*, z_*)$ can be written as

$$\frac{\partial \mathcal{M}_*}{\partial \mathcal{M}} \frac{\partial z_*}{\partial z} = \frac{D'(z)}{D'(z_*)} \frac{1+z}{1+z_*} \sqrt{\mu}. \tag{6.12}$$

Rates

We write the observed rate of merger events per unit redshift and unit chirp mass as:

$$r^{(GW)}(\mathcal{M}, z) = \frac{R(\mathcal{M}, z)}{1+z} \mathcal{E}_L^{(GW)}(\mathcal{M}, z), \tag{6.13}$$

where R is the intrinsic rate in the source frame, and $\mathcal{E}_L$ the lensing boost. Here, we separate the rate into two components:

$$R(\mathcal{M}, z) = R(\mathcal{M}) R(z), \tag{6.14}$$

and, for the redshift-dependent part, we assume a rate which is proportional to the product of the comoving volume boosted by a factor $(1+z)^\beta$:

$$R(z) \propto \frac{dV_c}{dz} (1+z)^\beta \propto \frac{d_L^2(z)}{E(z)} (1+z)^{\beta-2}, \tag{6.15}$$

where we use a standard ΛCDM cosmology with $E(z) = \sqrt{0.3(1+z)^3 + 0.7}$. This power-law behavior is expected if the merger rate of compact binary objects traces the star formation history (Madau et al., 1998) at low redshift (Dominik et al., 2013). In this toy model, we also invert the sign of the power-law index $\beta = 2.3$ at $z = 2$, in order to simulate a peak in the star formation rate.

Similar expressions can also be written for the rates of SNIa and the number counts of quasars:

$$r^{(SN)}(z) = \frac{R(z)}{1+z} \mathcal{E}_L^{(SN)}(z), \tag{6.16}$$

$$n^{(Q)}(\mathcal{L}, z) = N(\mathcal{L}) \mathcal{E}_L^{(Q)}(\mathcal{L}, z). \tag{6.17}$$

Even though we assume that the intrinsic luminosity function of quasars $N(\mathcal{L})$ is not redshift dependent, lensing effects introduce this dependence in the observed $n(\mathcal{L}, z)$. The lensing boost factors can then be written as:

$$\mathcal{E}_L^{(GW)} = \int d(\mathcal{M}_*/\mathcal{M}) \ \frac{R(\mathcal{M}_*)}{R(\mathcal{M})} W^{(GW)}(\mathcal{M}_*/\mathcal{M}, z), \tag{6.18}$$

$$\mathcal{E}_L^{(SN)} = \int dD_* \ \frac{R(z_*)}{R(z)} W^{(SN)}(D_*/D, z), \tag{6.19}$$

$$\mathcal{E}_L^{(Q)} = \int d\log_{10}(\mathcal{L}_*/\mathcal{L})\ \frac{N(\mathcal{L}_*)}{N(\mathcal{L})} W^{(Q)}(\mathcal{L}_*/\mathcal{L}, z), \tag{6.20}$$

where we have introduced the weight functions W^X, quantifying the contribution to the observed rates at $z, \mathcal{M}, \mathcal{L}$ from lensed events. These weight functions can be written as the product of the following terms.

- A lensing term. For each $z_*, \mathcal{M}_*$ and $\mathcal{L}_*$, there is an associated lensing probability. For GW and SN, this is $P(\mu, z_*)$ because the measured redshift z, inferred from the luminosity distance, is different from the source redshift z_*. This probability is $P(\mu, z)$ for the Q case because it is measured directly. For $\mu > 3$, we have $P(\mu, z_*) > P(\mu, z)$, meaning that we expect strong lensing to be particularly efficient for standard candles/sirens. Furthermore, because the expressions above are not written as integrals in μ, this term also contains a probability volume, e.g. $d\mu/dz_*$ for the SN case.

- A comoving volume term for the GW and SN cases. This is due to our assumption that $R(z) \propto dV_c$. Because lensing introduces contributions from a redshift range different from the observed z, a term $dV_c(z_*)/dV_c(z)$ is present.

- A redshift evolution term for SN and GW. Similar to the previous case, except due to the assumed power-law dependence of $R(z)$. This term also accounts for the different redshifted rates and is equal to $\left(\frac{1+z_*}{1+z}\right)^{\beta-1}$.

- A Jacobian term. As introduced in the previous section, the lensing transformation from intrinsic to observed quantities introduces an additional Jacobian factor.

In the next section, we study the impact of lensing magnification on the inferred chirp mass and redshift values and compare these results to the EM cases. We will work with the arguments of the integrals written above and, for ease of readability, we will also normalize these functions w.r.t. their value at null magnification ($\mu = 1$). In particular, we chose not to focus extensively on the results of the integral $\mathcal{E}_L^{(GW)}$, since it strongly depends on the assumed mass function $R(\mathcal{M})$. For accurate rates, we refer the reader to previous works (e.g. Dai et al., 2017; Oguri, 2018; Broadhurst et al., 2018; Ng et al., 2018).

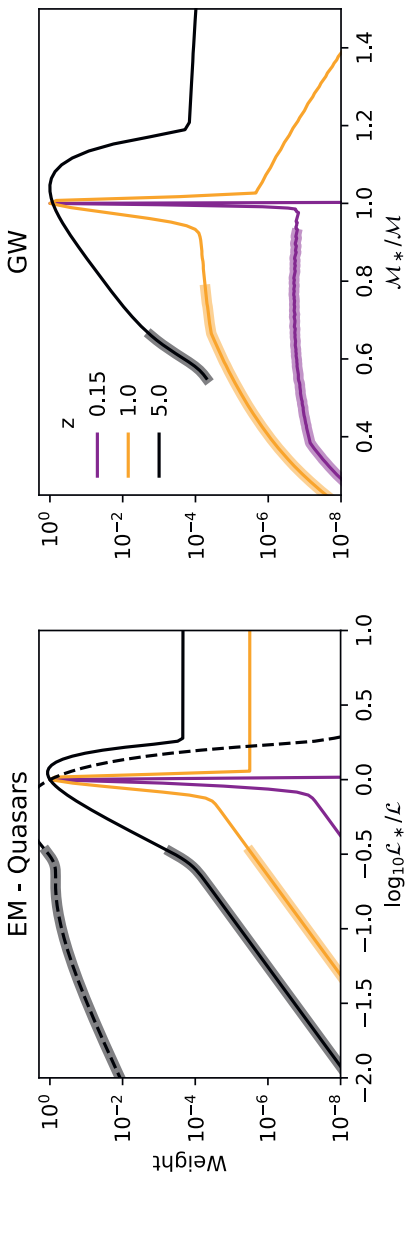

Figure 6.1: Relative contribution to the observed counts of transient GW events with chip-mass $\mathcal{M}$ or permanent EM sources with luminosity $\mathcal{L}$ by events with different intrinsic properties ($\mathcal{M}_*$ or $\mathcal{L}_*$). The observed redshift z is equal to the intrinsic one for the EM case. The filled lines assume a flat mass/luminosity function ($\mu > 3$ for the thick lines), while the dashed line corresponds to the weights for an observed luminosity located well past the knee of a Schechter luminosity function ($\mathcal{L}/\mathcal{L}_0 = 10$). For non-flat distributions, the relative contribution is the mass (or luminosity) function multiplied by these weights. see Eqs. (6.18) and (6.20).

6.2.2 Observational consequences

Weight functions

On the right side of Fig. 6.1, we plot the contribution of different intrinsic chirp masses to the integral in Eq. (6.18), while on the left-side we plot the equivalent result for light. These functions correspond to $W^{(GW)}$ and $W^{(Q)}$.

The first obvious conclusion is that magnification affects the inferred rates of GW mergers more efficiently than EM sources at both high and low redshift. This is mainly because GW lensing gives access to a broader volume at higher redshift, corresponding to a higher Jacobian factor and significantly stronger lensing probabilities. These effects are the main discriminant between the two cases and are dominant at low redshift.

We note, however, that the GW weights are still low. If we focus on a LIGO-like source ($z \sim 0.15$), we see that, to have rates at mass $\mathcal{M}$ dominated by events at $\mathcal{M}_* \sim \mathcal{M}/3$, the mass function $R(\mathcal{M})$ should span roughly 7 orders of magnitude between $\mathcal{M}_*$ and $\mathcal{M}$. While this is possible, we point out that this roughly corresponds to a doubly-exponential tail, with

$$R(M) \propto e^{-e^{\mathcal{M}/\mathcal{M}_0}} \tag{6.21}$$

and $\mathcal{M}_0 = \mathcal{M}_*$. This conclusion is mostly independent of our assumed mild redshift evolution.

Despite the lower lensing weights for the EM case, we also show that a typical Schechter function $N(\mathcal{L}) \propto \exp(-\mathcal{L}/\mathcal{L}_*)/\mathcal{L}$ (Schechter, 1976) is able to introduce a significant contribution from highly magnified sources at high z.

Lensing tail

In Fig. 6.2 we show the expected lensing tail of a truncated power-law distribution $R(\mathcal{M}) \propto \mathcal{M}^{-n}$ for a few choices of n. Events measured with a chirp-mass larger than the cut-off value $\mathcal{M} > \mathcal{M}_{\rm co}$ must be magnified mergers with intrinsic redshift $z_* > z$ and intrinsic chirp-mass $\mathcal{M}_* < \mathcal{M}$.

The prominence of this tail for a steep mass function (large n) and low redshift z explains why a source distribution can be designed to produce a large number of lensed events (Broadhurst et al., 2018). It is useful to stress here that the main reason behind this is not the larger volume available to be lensed, but the fact that higher redshift events contributing to the low redshift rates are both more likely to be lensed and are also *necessarily* located on a more abundant portion of the mass function. This is because the mapping $(\mathcal{M}, z) \leftrightarrow (\mathcal{M}_*, z_*)$ depends only on μ. Despite the main advantage of amplifying the lensing tail compared to the naive expectation, this mechanism has the drawback of being efficient only for events with low z. For example, the shape of the $z = 5$ lensing tail is less sensitive to the details of the mass function.

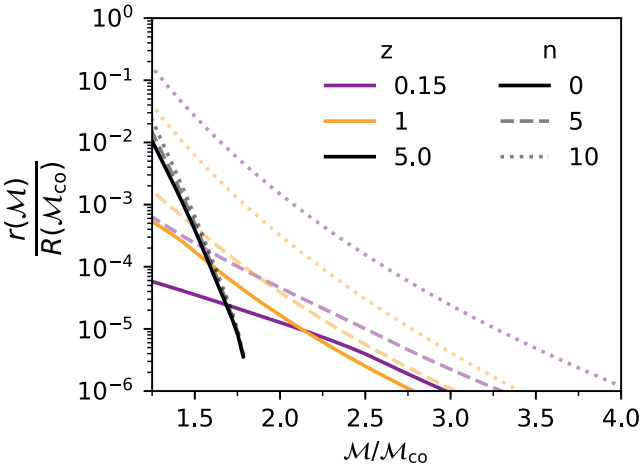

Figure 6.2: The shape of the lensing tail for truncated power-law distributions. The figure shows the observed rate $r(\mathcal{M})$ for an intrinsic chirp-mass function $R(\mathcal{M}) \propto \mathcal{M}^{-n}$ truncated at $\mathcal{M}_{\rm co}$. The observed rate for $\mathcal{M} > \mathcal{M}_{\rm co}$ must therefore be due to lensed events. The dependence on n is more striking for low inferred redshifts z due to how the intrinsic chip masses are distributed in the volume at $z_* > z$. See Section 6.2.2 for more details.

Here we do not assume a lower limit for the values $\mathcal{M}_*$, and the integrals are truncated because we impose $z_* < 10$. While this choice is unrealistic, it is possible to verify that setting a lower limit $\mathcal{M}_* > 5\ \mathrm{M}_\odot$ (1) does not affect the quantitative results of Fig. 6.2 for $n < 10$ and $\mathcal{M} > 20\ \mathrm{M}_\odot$, and (2) has no impact on the qualitative results discussed in this section for all values of n.

Luminosity distance

Another consequence of the dependence of the observed mass $\mathcal{M}$ on the magnification μ is the broadness of the peak in Fig. 6.1. The standard deviation of this distribution can be interpreted as an uncertainty in the measured $\mathcal{M}$, and, for an individual event, it can be pretty substantial: its value grows from 1 to about 7 percent between $z = 1$ and $z = 5$. The primary source of this scatter is the convergence distribution discussed in Section 6.2.1, and it is not particularly affected by our chosen source redshift dependence $R(z)$. For a flat mass function, no significant bias is observed in this redshift range, meaning that the contributors to an event of observed chirp mass $\mathcal{M}$ and redshift z are expected to have, on average, the same intrinsic properties.

This scatter also introduces an intrinsic error on the luminosity distance estimate to a source. For a flat mass function, we find a spread of 2.5 percent at $z = 0.15$ and 10 percent at redshift $z = 5$, which is consistent with results from previous works (e.g. Holz and Linder, 2005; Kocsis et al., 2006; Sathyaprakash et al., 2010; Oguri, 2016). However, this value should be compared to the present-day observational uncertainty in $D(z)$ of about 25 percent, dominated by the poorly constrained detector efficiency.

One can also find that in the presence of a steep mass function, the inferred $D(z)$ is substantially more biased compared to the inferred $\mathcal{M}$. This is because D_* and $\mathcal{M}_*$ scale differently with μ (Eq. 6.9 and 6.11).

6.2.3 Comparison to observations

LIGO-Virgo is expected to reach its design sensitivity in a few years. The expected statistical sample of mergers, made of hundreds or thousands of events, will allow a complete reconstruction of the chirp mass distribution of the underlying populations. If the intrinsic distribution is extremely peaked, the observed one might be contaminated by highly lensed events with biased luminosity distances and chirp masses. However, not only this scenario is in conflict with the expectation from current stellar evolution models (see e.g. Belczynski et al., 2016, 2017), but we have shown here that this would leave an easily recognizable signature in the LIGO rates due to (1) the wide range of probed masses at low redshift (Martynov et al., 2016) and (2) the flatness and low values of the lensing efficiency as a function of chirp mass (see Fig. 6.1).

As an example, the contribution to mergers with an observed $\mathcal{M} \sim 30\ M_\odot$ and $z \sim 0.15 - 1$ ($D \sim 700 - 1000$ Mpc) from events with lower $\mathcal{M}$ is suppressed by a factor $\sim 10^6 - 10^4$. No matter how these lensed events are distributed in intrinsic

chirp mass, the non-lensed events with similar properties should be both abundant and isolated from the highly suppressed lensing tail. Note that these properties roughly correspond to the 12 mergers detected during the first and second observing run of LIGO-Virgo (Abbott et al., 2019). This implies that the absence of a larger number of events at $\mathcal{M} < 10\ \mathrm{M}_\odot$ (to which the detector is sensitive) suggests that the observed events are not lensed.

6.3 The astrophysical background

6.3.1 Formalism

Autocorrelation

In this section, we discuss the autocorrelation signal of the anisotropic GWB. This signal and the shot-noise contamination have been extensively studied in previous works (Jenkins, Alexander C. and Sakellariadou, Mairi, 2019; Jenkins et al., 2019a; Cusin et al., 2019). Here, we review the main modeling aspects and describe some particularities.

Our starting point is the definition of the dimensionless energy density of GWs per unit solid angle from a given direction of the sky $\hat{\mathbf{r}}$. We model this signal as

$$\Omega_{\rm GW}(\hat{\mathbf{r}}) \equiv \int dr\ r^2 \mathcal{K}(r) n(\vec{\mathbf{r}}), \tag{6.22}$$

where $n(\vec{\mathbf{r}})$ is the galaxy density field in comoving coordinates $\vec{\mathbf{r}}$, and $\mathcal{K}$ is the GW kernel that encodes the average contribution of a galaxy to Ω_{GW} as a function of comoving distance r. In practice, this includes information about the star formation history of the Universe and the properties of the emitting binary population. It is instructive to rewrite Eq. (6.22) in terms of the galaxy overdensity $\delta_{\rm g}(\vec{\mathbf{r}}) \equiv n(\vec{\mathbf{r}})/\bar{n}(r) - 1$, with $\bar{n}(r)$ being the average number density of galaxies, defined as $\bar{n}(r) \equiv \int \mathrm{d}^2\hat{\mathbf{r}} n(\vec{\mathbf{r}})/4\pi$. With this notation we have

$$\Omega_{\rm GW}(\hat{\mathbf{r}}) = \int dr\ r^2 \mathcal{K}(r) \bar{n}(r) \left(\delta_{\rm g}(\vec{\mathbf{r}}) + 1\right). \tag{6.23}$$

From this point, the angular power spectrum of the anisotropic GWB $C_\ell^{\rm GW}$ can be calculated to be

$$C_\ell^{\rm GW} = 4\pi \int_{k_{\rm min}}^{k_{\rm max}} \frac{dk}{k} |\delta\Omega_\ell|^2 \mathcal{P}(k) + B_\ell^{\rm GW}. \tag{6.24}$$

Here $\delta\Omega_\ell(k)$ is given by

$$\delta\Omega_\ell(k) = \int dr\ r^2 \mathcal{K}(r) \bar{n}(r) T_g(k,r) j_\ell\left(kr\right), \tag{6.25}$$

where T_g is the synchronous gauge transfer function relating the galaxy power spectrum to the primordial one $\mathcal{P}(k) = A_s \left(k/k_*\right)^{n_s - 1}$, and j_ℓ is the spherical Bessel function of order ℓ. Note that the galaxy bias is implicitly absorbed in T_g. Note also that in Eq. (6.25) we neglect relativistic corrections, as they are generally found to be below cosmic variance (Bertacca et al., 2019).

The term $B_\ell^{\rm GW}$ in the power spectrum is the shot-noise bias term introduced by the spatial and temporal shot-noise in the distribution of the individual events forming the GWB. Following Jenkins, Alexander C. and Sakellariadou, Mairi (2019), we write the shot-noise contribution in the kHz band as

$$B_\ell^{\rm GW} = \int dr\, \mathcal{K}^2(r) \bar{n}(r) r^2 \left[1 + \frac{1+z(r)}{R(r) T_O}\right]. \tag{6.26}$$

Because of the low event rate in this frequency range, this noise contribution is inversely proportional to the average number of events per galaxy, written as the average redshifted event rate $R(r)/(1+z)$ multiplied by the observing time T_O. However, because the duration of the inspiral phase in the mHz band is much larger than any reasonable observing time, the contribution of the term $1/(R(r)T_0)$ is negligible in this case.

The GWB discussed here is an integrated signal. Because of this, the low-redshift objects might significantly contribute to the GWB. Indeed, the astrophysical models of Cusin et al. (2019) suggest that the combination

$$\tilde{\mathcal{K}}(r) = \mathcal{K}(r) \bar{n}(r) r^2 \tag{6.27}$$

is not decaying to negligible values close to redshifts $z \sim 0$. This introduces two complications in the modelling.

The first is connected to the shot noise. To highlight this, we rewrite Eq. (6.26) as

$$B_\ell^{\rm GW} = \int dr\, \frac{\tilde{\mathcal{K}}^2(r)}{\bar{n}(r) r^2} \left[1 + \frac{1+z(r)}{R(r) T_O}\right]. \tag{6.28}$$

This expression shows that the shot-noise has a divergent expression due to low-redshift (low-r) contributions. This divergence can be suppressed if local events are excluded from the background to obtain a well-behaved prediction for the autocorrelation signal. This is equivalent to setting a lower limit in the integral above different from zero.

Second, there is a complication derived from the scale-dependent part of the angular power spectrum (the first term in Eq. (6.24)), which is expected to receive non-negligible contributions from small, highly non-linear scales. To get some intuition about this feature, let us simplify our expression for the GWB angular power spectrum by using the so-called Limber approximation

$$j_\ell(x) \to \sqrt{\frac{\pi}{2\alpha}} \delta_{\rm D}\left(\alpha - x\right), \tag{6.29}$$

where $\delta_{\rm D}$ is the Dirac delta-function and $\alpha \equiv \ell + 1/2$. Using this in Eq. (6.25) and neglecting the bias term we obtain

$$C_\ell^{\rm GW} \approx \frac{2\pi^2}{\alpha} \int_{k_{\rm min}}^{k_{\rm max}} \frac{{\rm d}k}{k^3} \tilde{\mathcal{K}}^2 \left(\frac{\alpha}{k}\right) \mathcal{S}^2 \left(k, \frac{\alpha}{k}\right), \tag{6.30}$$

$$\mathcal{S}(k, r) \equiv T_g(k, r) \mathcal{P}(k)^{1/2}. \tag{6.31}$$

What Eq. (6.30) demonstrates is that $\tilde{\mathcal{K}}(r)$ acts as a modified kernel and selects a particular domain in the k-integral. This causes small scales to contribute significantly to $C_\ell^{\rm GW}$, unless $\tilde{\mathcal{K}}$ is vanishing at the lower end of its argument or $\tilde{\mathcal{S}}^2/k^3$ is falling fast enough at large values of k. As the modeling of the galaxy power spectrum at non-linear scales is highly uncertain, this feature signals a potential danger of using the autocorrelation signal as a probe of the GW merger history or cosmology.

Cross-correlation with galaxy clustering

This subsection introduces the main concepts necessary for modeling the cross-correlation signal and discusses its advantages. First of all, we define the observed overdensity of galaxies in the given direction $\hat{\mathbf{r}}$ per unit sold angle as

$$\Delta(\hat{\mathbf{r}}) = \int dr\ W_i(r) \delta_g(\vec{\mathbf{r}}), \tag{6.32}$$

where $W_i(r)$ is the probability density function of the galaxies' comoving distances (also referred to as the *window function*) and $\delta_g(\vec{\mathbf{r}})$ is the galaxy overdensity defined earlier. Using Eq. (6.32), the angular power spectrum of this field, $C_\ell^{\rm GC}$, can be shown to be

$$C_\ell^{\rm GC} = 4\pi \int \frac{dk}{k} |\Delta_\ell(k)|^2 \mathcal{P}(k) + \frac{1}{n_i}, \tag{6.33}$$

where $\Delta_\ell(k)$ is given by

$$\Delta_\ell(k) = \int dr\ W_i(r) T_i(k, r) j_\ell(kr). \tag{6.34}$$

$T_i(k, r)$ is the transfer function for the galaxy overdensity in the selected redshift range $W_i(r)$, $j_\ell(kr)$ is the spherical Bessel function of order ℓ and n_i is the average number of galaxies per steradian, also dependent on the specific redshift selection $W_i(r)$. This final quantity appears in the second term in Eq. (6.33) and dictates the size of the shot-noise component of the power spectrum. In total, the spectrum $C_\ell^{\rm GC}$ as a function of scale ℓ is also sometimes referred to as the galaxy clustering (GC) angular power spectrum.

Using Eqs. (6.25) and (6.34), one can derive the angular power spectrum of the cross-correlation $C_\ell^\times$ of the GWB and the GC maps, given by Eq. (6.22) and (6.32). This is

$$C_\ell^\times = 4\pi \int \frac{dk}{k}\, \delta\Omega_\ell^*(k) \Delta_\ell(k) \mathcal{P}(k) + B_\ell, \tag{6.35}$$

where the shot-noise contribution B_ℓ, derived in Appendix 6A, can be shown to be

$$B_\ell = \int dr\; W_i(r) \mathcal{K}(r). \tag{6.36}$$

With these expressions in mind, we can now discuss how the cross-correlation signal can address the modeling challenges presented in the previous section.

To address the first one, we notice that, while the $1/r^2$ divergence is still present in the integral in Eq. (6.36), this integral is generally well behaved if the window function $W_i(r)$ decays fast enough at small redshifts. Notice that this is impossible to do in the equivalent expression for the autocorrelation in Eq. (6.26).

With respect to the second issue related to the small-scale dependence of the signal, we write the equivalent of Eq. (6.30) for the cross-correlation,

$$C_\ell^\times \approx \frac{2\pi^2}{\alpha} \int_{k_{\rm min}}^{k_{\rm max}} \frac{\mathrm{d}k}{k^3} W_i\left(\frac{\alpha}{k}\right) \tilde{\mathcal{K}}\left(\frac{\alpha}{k}\right) \mathcal{S}^2\left(k, \frac{\alpha}{k}\right). \tag{6.37}$$

Because GC surveys allow for redshift-selection of the sources, the GC window function $W_i(r)$ can be taken to be peaked at some non-zero redshift and quickly decaying for larger or smaller values of r. Eq. (6.37) proves that this behavior cuts off the contribution from very large and very small scales.

6.3.2 Forecast

Model set-up

In this section, our primary goal is to explore the sensitivity of the cross-correlation signal to various parameters and estimate its information content. To this end, we model the signal using simple but representative assumptions about the GW and GC maps. This allows us to derive an upper limit on the constraining power by assuming the minimum theoretical uncertainty due to cosmic variance.

We base our model for $\tilde{\mathcal{K}}(r)$ on the physically motivated one of Cusin et al. (2019), by noting that their function $\mathcal{A}(z)$ is the analogue of our $\tilde{\mathcal{K}}(r)$ in redshift space. In this reference, in particular, it is shown that $\mathcal{A}(r)$ is a slowly-evolving function of redshift and has a similar shape over a wide range of frequencies and assumptions about the source population (see their figures 19 and 13). Thus, we model the kernel as

$$\mathcal{K}(r) = \frac{\mathcal{K}_0}{2\bar{n}(r) r^2} \left\{\tanh\left[10(z_*(r) - z(r))\right] + 1\right\}, \tag{6.38}$$

where $\mathcal{K}_0$ is the amplitude of the kernel, z_* is a cut-off redshift, and $\bar{n}(r) \approx 10^{-1}$ Mpc^{-3} is the average comoving galaxy number density estimated using Figure 4 of Schaye et al. (2015). We do not implement a redshift dependence for this quantity because its value is relevant only for the shot-noise component of the cross-correlation, found to be negligible in the cases considered here. In our fiducial model, we assume $z_* = 1$ as the astrophysical kernel $\mathcal{K}(r)\bar{n}(r)r^2$ is expected to decay around that value in redshift. Notice that, while $\mathcal{K}_0$ should be dimensionful, its units are irrelevant to us because the cross-correlation signal is proportional to its value. For the rest of the section, we call $\mathcal{K}_0^{\rm fid}$ the fiducial value of this quantity.

In the next subsections, we study the cross-correlation between the GWB modeled above and two galaxy catalogs centered at different redshifts. The two window functions, W_1 and W_2, are assumed to be Gaussian distributions centered at $\bar{z} = \{0.5, 1.5\}$ and with widths of $\sigma_z = \{0.18, 0.6\}$. These values are picked so that the two selections overlap with the constant portions of $\tilde{\mathcal{K}}(r)$.

Moreover, we model the transfer functions in Eqs. (6.34) and (6.25) by using a linear bias approximation (valid for large scales):

$$T_i(k) = b_i T_{\rm m}(k, r), \tag{6.39}$$

and

$$T_g(k, r) = b_{\rm GW} T_{\rm m}(k, r), \tag{6.40}$$

where $T_{\rm m}(k, r)$ is the transfer function for cold dark matter, and the b_X are known as bias parameters. When varying our model, we freeze the bias of both galaxy catalogs since it can be extracted from their clustering autocorrelation signal alone. On the contrary, we treat the GW bias $b_{\rm GW}$ as a free parameter, and we assume it to be a constant over redshift. While this is not necessarily true, in the absence of shot-noise, only the combination $b_{\rm GW}\tilde{\mathcal{K}}(r)$ appears in the signal. This implies that a more complex model can always capture any redshift dependence through the function $\tilde{\mathcal{K}}(r)$. Note, however, that breaking the degeneracy between the linear bias of the GW population and the amplitude of the astrophysical kernel $\mathcal{K}(r)$ requires a full understanding of the GWB kernel and all ingredients (Scelfo et al., 2018b).

We focus on the mHz frequency band for the rest of the analysis and assume that low-redshift events (below $r = 150$ Mpc) can be filtered. As discussed in the previous sections, these assumptions are essential to obtain a well-behaved signal not overwhelmed by noise. For reference, under these assumptions, we get the following relative noise values at $\hat{\ell} = 10$:

$$\frac{B_{\hat{\ell}}^{\rm GW}}{C_{\hat{\ell}}^{\rm GW}} \approx \frac{B_{\hat{\ell}}}{C_{\hat{\ell}}^{\times}} \approx 10^{-4}. \tag{6.41}$$

This value is derived using the inspiral time of a solar mass black hole binary starting

from 1 mHz (Blanchet et al., 1995), an observing time of 1 year and a merger rate of 10^{-5} per year.

The codes used in this section are made publicly available on https://github.com/valerivardanyan/GW-GC-CrossCorr. To calculate the matter power-spectra we use the ΛCDM limit of EFTCAMB (Hu et al., 2014; Raveri et al., 2014).

Constraining $\mathcal{K}(r)$

The main goal of this section is to understand the constraining power of the cross-correlation signal by studying how precisely the astrophysical model can be inferred from a noisy C_ℓ measurement.

In our analysis, we focus on the best-case scenario of cosmic-variance limited uncertainties as derived in Appendix 6B and use a simple proxy for the overall signal-to-noise ratio of the cross-correlation, defined as

$$\left(\frac{\mathrm{S}}{\mathrm{N}}\right)^2 \equiv \sum_{\ell=\ell_{\rm min}}^{\ell_{\rm max}} \frac{\left(C_\ell^\times\right)^2}{\mathrm{Var}C_\ell^\times}. \tag{6.42}$$

Let us note that in our setup, the GC signal dominates over the GC shot noise, implying that Eq. (6.42) is indeed the theoretical limit for uncertainties. In the presence of multiple, independent window functions, we simply sum the relative signal-to-noise expressions in quadrature.

We compute the cross-correlation power spectra, given in Eq. (6.35), using the model presented in Section 6.3.2, and attempt to recover the model parameters from a noisy realization. To explore the inferred constraints as a function of angular resolution and S/N levels, we do this in several multipole ranges of ℓ with $\ell_{\rm min} = 2$ and varying $\ell_{\rm max}$.

The parameters of interest in our analysis are the amplitude of the GWB kernel $\mathcal{K}_0$ and the turnover redshift z_*. In addition to these, we also explore the bias $b_{\rm GW}$ and $\Omega_{\rm m}$ to see if variations in $T_g(k,r)$ can affect the inferred $\mathcal{K}(r)$, and to explore the possible degeneracies between the GWB model and cosmology. To include the effects of varying $\Omega_{\rm m}$ we have precomputed the dark matter transfer functions for a grid of $\Omega_{\rm m}$ values and have inferred the results for the intermediate values through nearest-neighbor interpolation. We have employed a Gaussian likelihood function on C_ℓ with diagonal covariance matrix given through Eq. (6.77), and the prior ranges shown in Table 6.1. Note that since we expect $\mathcal{K}_0$ to be degenerate with $b_{\rm GW}$, we do not vary $\mathcal{K}_0$ itself, but rather vary the combination $b_{\rm GW}\mathcal{K}_0$.

The main results of the analysis are summarised in Fig. 6.3, where we show the expected constraints on the parameters of interest as a function of the maximum multipole included in the analysis. We also offer the corresponding cosmic-variance-only signal-to-noise ratios.

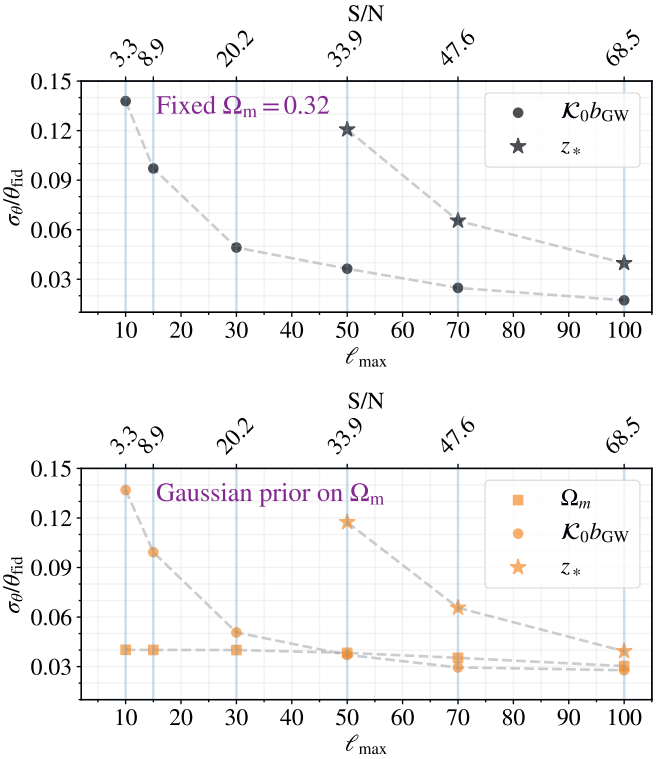

Figure 6.3: Constraints on the GWB parameters ($b_{\rm GW}\mathcal{K}_0$, z_*) and cosmology (Ω_m) obtained using the cross-correlation signal with two window functions as a function of the maximum multipole included in the analysis. Cosmic-variance limited measurements are assumed for all the constraints, so these should be understood as the best-case scenario results. Larger values of the signal-to-noise ratio (S/N) correspond to better angular resolution (see Eq. 6.42). We have explored the effect of $\Omega_{\rm m}$ on these constraints by either fixing its value (***top panel***), or setting a Planck-2018-like Gaussian prior (***bottom panel***). Remarkably, the combination $b_{\rm GW}\mathcal{K}_0$ can be constrained even with very limited angular sensitivity. The turnover location z_* is practically unconstrained for $\ell_{\rm max} \lesssim 50$, and $\Omega_{\rm m}$ is prior dominated for these multipoles. In case of $\ell_{\rm max} \gtrsim 50$ all the relevant parameters are tightly constrained, and for $\ell_{\rm max} \sim 100$ the constraints are at the level of a few percent. Notably, the cosmology (mimicked by varying $\Omega_{\rm m}$ in our analysis) can match and surpass the CMB results only in case of high angular resolution/signal-to-noise. For reference, $\ell_{\rm max} = 100$ roughly corresponds to 2 degrees.

Parameter	Fiducial value	Prior
$b_{\rm GW}\mathcal{K}_0$	1	$[0.01, 100]$
$b_{\rm GW}$	1	$[0.1, 10]$
z_*	1	$[0.5, 1.5]$
$\Omega_{\rm m}$	0.32	$\mathcal{G}(0.32, 0.013)$

Table 6.1: Prior ranges of the sampled parameters. For $\Omega_{\rm m}$ we use a Planck-2018 inspired Gaussian prior.

Let us first have a look at the top panel of the figure, which corresponds to a fixed $\Omega_{\rm m}$ value. As we see, $b_{\rm GW}\mathcal{K}_0$ is constrained and, notably, this is true even in the limited multipole range corresponding to $\ell_{\rm max} = 10$. This is expected, as a clear signal detection is associated with a measurement of its amplitude. On the other hand, less encouraging are the results for the turnover redshift z_*, which can be constrained only for $\ell_{\rm max} \gtrsim 50$ or, equivalently, an S/N of ~ 33. In the bottom panel of the figure, we now impose a Gaussian prior on $\Omega_{\rm m}$, with its variance being comparable to the Planck-2018 constraint on $\Omega_{\rm m}$. While the z_* results are not affected, the uncertainties on the amplitude are now slightly inflated due to a degeneracy between $\Omega_{\rm m}$ and $b_{\rm GW}\mathcal{K}_0$.

Let us now fully concentrate on the two limiting angular sensitivities in our analysis. The turn-over redshift z_* is unconstrained for the low-resolution case, while it is tightly constrained for the case of $\ell_{\rm max} = 100$. The dark matter abundance $\Omega_{\rm m}$ is prior dominated for the low-resolution case, while it beats the prior in the high-resolution scenario.

Before turning to the next section, we want to mention that the results presented in this section depend on the precise details of the GC window functions and GWB detection, and more accurate results can only be obtained by performing a realistic forecast with exact survey/detector specifications. While we leave a more detailed investigation for future research, our results suggest that a cosmic-variance limited measurement of the GWB anisotropies down to $\ell \sim 100$ can tightly constrain the redshift evolution of the GW kernel $\tilde{\mathcal{K}}$.

6.4 Resolved events

6.4.1 Formalism

Gravitational wave propagation

In GR, the amplitude of GWs on top of Friedmann-Lemaitre-Robertson-Walker (FLRW) background evolves according to

$$h''_\alpha + 2\mathcal{H}h'_\alpha - \vec{\nabla}^2 h_\alpha = 0, \tag{6.43}$$

where h_α denotes the amplitude of either polarization ($\alpha \in [\times, +]$), primes denote derivatives with respect to the conformal time, and $\mathcal{H}$ is the conformal Hubble function. In this equation, the prefactor of the Laplacian term controls the propagation speed, which we have set to coincide with the speed of light in $c = 1$ units.

The second term is the standard cosmic friction term and its impact, combined with conservation of gravitons, causes the strain amplitude to decay as $h_\alpha(z) \propto D_{\rm L}^{-1}(z)$, with D_L being the FLRW luminosity distance:

$$D_{\rm L}(z) = (1+z)\int_0^z \frac{{\rm d}\tilde{z}}{H(\tilde{z})}, \tag{6.44}$$

where the Hubble function $H(z)$ is given in terms of the Hubble constant H_0, present-day dark matter abundance $\Omega_{\rm m}$ and dark energy abundance $\Omega_{\rm DE}(z)$ as

$$H(z) = H_0\left[\Omega_m(1+z)^3 + \Omega_{DE}(z)\right]. \tag{6.45}$$

Throughout this section we assume a constant equation of state w_0 for dark energy, such that its energy density is given by

$$\Omega_{DE}(z) = (1-\Omega_{\rm m})(1+z)^{3(1+w_0)}. \tag{6.46}$$

The standard ΛCDM cosmology corresponds to $w_0 = -1$.

It is now established that modifications of GR can affect the propagation of GWs. The important effect for us is the modified friction term with respect to the GR expectation in Equation (6.43),

$$h''_\alpha + \left[2 + \alpha_M(z)\right]\mathcal{H}h'_\alpha - \vec{\nabla}^2 h_\alpha = 0, \tag{6.47}$$

where we have introduced an additional function α_M modelling this change. Once again, we imposed the GW speed to be unity as suggested by observations. The modified friction term introduces a new scaling $h_\alpha(z) \propto 1/D_{\rm L,GW}(z)$, with $D_{\rm L,GW}(z) \neq D_{\rm L}(z)$ for non-zero $\alpha_M(z)$. The luminosity distance to GW events can be written as:

$$\frac{D_{\rm L,GW}}{D_{\rm L,EM}}(z) = \exp\left\{-\frac{1}{2}\int_0^z {\rm d}\tilde{z}\,\frac{\alpha_M(\tilde{z})}{(1+\tilde{z})}\right\}. \tag{6.48}$$

In this work, we assume that the luminosity distance for EM sources $D_{\rm L,EM}$ is unaffected and is equal to the expression in Equation (6.44). The function α_M corresponds to the running of the effective Planck mass, i.e.,

$$\alpha_M = \frac{d\log(M_{\rm eff}/M_{\rm P})^2}{d\log a}, \tag{6.49}$$

where $M_{\rm P}$ is the Planck mass and $M_{\rm eff}$ is its effective value at redshift $z = 1/a - 1$. This function encodes information about extensions of GR such as scalar-tensor theories

that predict the existence of a gravitational scalar degree of freedom non-minimally coupled to curvature (Horndeski, 1974; Bellini and Sawicki, 2014). This scalar degree of freedom can also propagate as a scalar wave. Still, its effects are expected to be suppressed on Earth, where local tests of gravity place tight constraints on deviations from GR (see e.g. Bertotti et al., 2003). However, notice that this restoration of the GR limit does not impact the effect discussed here, Eq. (6.48) is an integrated effect, and the impact of the local region of observation is minimal. More broadly, it should be noted that this modified friction term is also a natural prediction of quantum gravity (Calcagni et al., 2019) and non-local modifications of gravity (Dirian et al., 2016).

From an effective field theory point of view, $\alpha_M(z)$ is a free function of order unity. However, in practical studies of modified gravity and dark energy, α_M is often assumed to take simple parametric forms. The main guiding principle is the assumption that its effects should be negligible in the early universe, which prompts to choose $\alpha_M(z)$ to be proportional either to the dark energy abundance or simply to some power of the scale factor a.

Such parametrizations make it possible to find a closed form expression for the ratio in Equation (6.48) and have inspired a widely used parametrization of the ratio as a monotonic deviation which goes to 1 at present day (Belgacem et al., 2018)

$$\frac{D_{\mathrm{L,GW}}}{D_{\mathrm{L,EM}}}(z) = \Xi_0 + \frac{1-\Xi_0}{(1+z)^n}. \tag{6.50}$$

In this expression, Ξ_0 and n are two constant parameters typically ~ 1.

Angular power-spectra

We consider GW mergers with a distribution in redshift written as

$$n_{\mathrm{GW}}(z) = \frac{n_0}{1+z}, \tag{6.51}$$

where n_0 corresponds to the comoving number density of observed events as a function of redshift, and the term $(1+z)$ takes into account the cosmological time dilation. In our analysis for this section, we use a constant value of $n_0 \approx 3\times 10^{-6}\ h^3\mathrm{Mpc}^{-3}$ (with h denoting here the usual normalized Hubble constant), motivated by current LIGO constraints (Abbott et al., 2020).

For a given selection of sources along the line of sight, the average number of projected sources can be written using the comoving distance $\chi(z)$:

$$\bar{n}_{\mathrm{gw}} = \int_0^\infty dz \frac{\chi^2(z)}{H(z)} S(z) n_{\mathrm{GW}}(z). \tag{6.52}$$

The function S encodes the selection, and the scatter due to observational errors. In this section, simple bins in a range $[D_{\mathrm{L,min}}, D_{\mathrm{L,max}}]$ are used and we assume a log-normal distribution with fixed scatter $\sigma_{\ln D}$ for the individual sources (Oguri, 2016). In

this case, S can be written as:

$$S(z) = \frac{1}{2}\left[x_{\rm min}(z) - x_{\rm max}(z)\right], \tag{6.53}$$

with

$$x_{\rm min}(z) = {\rm erfc}\left[\frac{\ln D_{\rm L,min} - \ln D_{\rm L,GW}(z)}{\sqrt{2}\sigma_{\ln D}}\right], \tag{6.54}$$

and similarly for $x_{\rm max}$. Including this effect makes S resemble a top-hat function with damping tails dictated by $\sigma_{\ln D}$.

The angular power spectrum of these sources can be written using the Limber approximation

$$C_{\rm GW}(\ell) = \int_0^\infty dz\, \frac{H(z)}{\chi^2(z)} W^2_{\rm GW}(z) b^2_{\rm GW}(z) P\left(\frac{\ell+1/2}{\chi(z)}, z\right), \tag{6.55}$$

where $P(k,z)$ is the matter power-spectrum at redshift z and comoving scale k, $b_{\rm GW}$ is the bias of the GW sources, and the window function can be written as

$$W_{\rm GW}(z) = \frac{\chi^2(z)}{H(z)} \frac{n_{\rm GW}(z)}{\bar{n}_{\rm GW}} S(z). \tag{6.56}$$

For the purpose of illustration, we will make use of a few simple parametrization for the GW bias. We will consider either a constant bias $b_{\rm GW}$ with a value of order unity or a more complex form:

$$b_{\rm GW}(z) = b_0\left(1 + \frac{1}{D(z)}\right), \tag{6.57}$$

where $D(z)$ represents the growth factor. The first model, with its low constant value, mimics a PBH origin for the mergers (Bird et al., 2016; Raccanelli et al., 2016), while the second mimics the stellar evolution case by tracking the galaxy linear bias (Oguri, 2016).

Similarly to the GW population, we again assume a constant comoving number density of galaxies. Throughout our analysis we fix

$$n_{\rm gal}(z) = 10^{-3} h^3 {\rm Mpc}^{-3}, \tag{6.58}$$

and we write the autocorrelation signal of galaxies under the Limber approximation as

$$C_{\rm gal}(\ell) = \int_0^\infty dz\, \frac{H(z)}{\chi(z)^2} W^2_{\rm gal}(z) b^2_{\rm gal}(z) P\left(\frac{\ell+1/2}{\chi(z)}, z\right). \tag{6.59}$$

In this expression the definition of $W_{\rm gal}$ is the same as $W_{\rm GW}$ used in the previous section except for using $n_{\rm gal}(z)$, a different selection function, and $b_{\rm gal}(z)$ is the linear galaxy bias. In our analyses, we assume a known galaxy bias in the form of

$$b_{\rm gal}(z) = 1 + \frac{1}{D(z)}. \tag{6.60}$$

In general, this function is expected to be accurately measured from the galaxy auto-correlation signal alone.

In this section, we employ a top-hat selection function for $W_{\rm gal}$, which assumes no uncertainty in galaxy redshift estimates. This choice mimics a spectroscopic galaxy survey or a general redshift survey with negligible uncertainties. As an example, another choice commonly found in the literature is a Gaussian distribution $\mathcal{N}(z, \sigma_{\rm gal})$, where $\sigma_{\rm gal}$ should be much larger than the expected redshift uncertainty for each galaxy.

By combining the distribution of GW sources and galaxies, one can construct a cross-correlation map. In our formalism, we write the cross-correlation between a GW bin i and a galaxy bin j (fully specified by their respective window functions) as:

$$C_{\times}^{ij}(\ell) = \int_0^{\infty} {\rm d}z \frac{H(z)}{\chi^2(z)} W_{\rm GW}^i(z) W_{\rm gal}^j(z) \times b_{\rm GW}(z) b_{\rm gal}(z) P\left(\frac{\ell + 1/2}{\chi(z)}, z\right). \tag{6.61}$$

Note that this signal is different from the GWB cross-correlation of Eq. (6.35) from the previous section.

We conclude this subsection by pointing out that the power spectra in Equations (6.59), (6.55) and (6.61) do not include relativistic terms and do not capture the effects of evolution and lensing bias (see e.g. Scelfo et al., 2018a, 2020, for a detailed treatment). Specifically, while the lensing bias should be negligible compared to the luminosity distance uncertainties at the redshifts considered here (see Section 6.2), the same is not true for relativistic effects. Therefore, we choose not to consider small values of ℓ in the analysis of this section since the signal at these large angular scales is largely dictated by them.

Constraining the propagation

The primary goal of the subsection is to demonstrate how to reconstruct the properties of GW propagation and source clustering as a function of redshift. We show how to recover an assumed fiducial model using mock angular power spectra with cosmic-variance or shot-noise limited uncertainties.

Our methodology hinges on the fact that by cross-correlating a GW luminosity distance bin with multiple galaxy redshift bins, we can determine the redshift of the GW sources by matching the clustering properties of the two at the true redshift (Oguri, 2016; Bera et al., 2020).

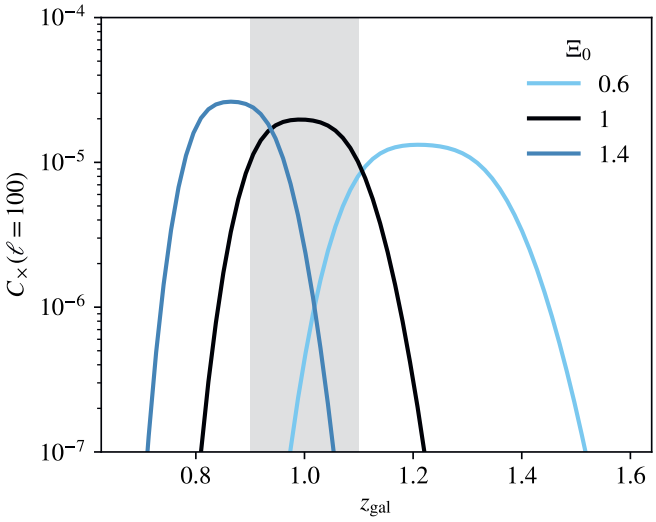

Figure 6.4: The cross-correlation signal between GW sources at $z = [0.9, 1.1]$ (shaded area) and galaxies at different redshifts ($z_{\rm gal}$). If the luminosity distance ratio $D_{\rm L,GW}/D_{\rm L,EM}(z)$ in Equation (6.50) is different from its GR assumption ($\Xi_0 \neq 1$), the location of the predicted cross-correlation peak is also affected.

We demonstrate this idea in Figure 6.4, where we have considered GW sources located at redshift $[0.9, 1.1]$ in a GR cosmology where $D_{\rm L,GW}(z) = D_{\rm L,EM}(z)$. This figure shows the expected cross-correlation signal between the angular distribution of these sources and the angular distribution of galaxies located at various redshifts. As expected, in GR ($\Xi_0 = 1$), the signal peaks inside the correct redshift range (shaded area). However, as we depart from the GW luminosity distance relation, the location of this peak is affected.

6.4.2 Forecast

Model set-up

In this section, we describe the recipe used to generate the mock angular power spectra ($C_{\rm gal}, C_{\rm GW}$, and $C_\times$) that are fed into our reconstruction pipeline together with their error covariance matrix. These angular power-spectra are extracted from the autocorrelation and cross-correlation maps representing the sky distribution of galaxies and GW sources when describing actual data. The recipe has three main ingredients: the details of the fiducial model, a description of the instrumental configuration and a definition of the dominant source of error.

The first ingredient is the fiducial model. Our decision in this case is based on the results of Baker and Harrison (2021), where present-day constraints on the function α_M appearing in Equation (6.48) are presented. As shown in Belgacem et al. (2019), the results of the $\alpha_M \propto a$ parametrization found in that work can be mapped to the $\Xi(z)$ function in Equation (6.50). Using this transformation, we find that the 3σ upper limit roughly corresponds to

$$\Xi_0 \lesssim 1.4, \tag{6.62}$$

with $n = 1$. Thus, we assume a fiducial model with $\Xi_0^{\rm fid} = 1.4$ and $n^{\rm fid} = 1$, representing the limit of our present understanding.

The second ingredient of our forecast is the instrumental configurations. The size of our data vector is given by the number of multipoles ℓ and window functions that we include in our analysis. Since both are primarily dictated by observational considerations, in this work, we assume an optimistic combination of a network of three Einstein Telescopes (Maggiore et al., 2020b; Hall and Evans, 2019) capable of a log-scatter in measured $D_{\rm L,GW}$ of $\sigma_{\ln D} = 0.05$, and a high-z redshift survey with extensive sky coverage and negligible redshift uncertainties (such as, e.g., the Square Kilometer Array, Weltman et al., 2020).

The range of angular scales that we consider is limited by two factors. On small scales, large multipoles ($\ell > 100$) are excluded due to the angular resolution of about 1 degree expected for our GW detector configuration of choice (Hall and Evans, 2019). On large scales, we do not explore values of $\ell < 10$ because our modeling does not consider the relativistic effects dominating the signal at these scales. Nevertheless, we

Parameter	Prior
Node amplitudes	[0, 11] (Uniform)
Correlation length (L)	[1, 10] (Uniform)
Ω_m	1% (Gaussian)
h	1% (Gaussian)
w_0	5% (Gaussian)

Table 6.2: Summary of the priors imposed before reconstructing $b_{\rm GW}/b_{\rm gal}\,(z)$ and $D_{\rm L,GW}/D_{\rm L,EM}\,(z)$ using 4 nodes each. The GP hyper-parameters (i.e., the 2 correlation lengths and the 4×2 amplitudes) are explored independently. The fiducial model is given by $\Xi_0 = 1.4, n = 1, \Omega_{\rm m} = 0.31, h = 0.67, w_0 = -1$.

stress that these multipoles contribute relatively little information compared to larger multipoles since they are dominated by cosmic variance.

Our window functions are distributed in the redshift range $[0.1, 3]$. We assume $N_{\rm gal} = 12$ galaxy bins equally spaced in redshift, and $N_{\rm GW} = 8$ GW luminosity distance bins equally spaced in $D_{\rm L,GW}$. We mention in particular that this choice is not completely arbitrary. The number of GW bins is motivated by forcing well-defined bins such that their width is at least three times the luminosity distance uncertainty $\sigma_{\ln D}$ that we have assumed. Furthermore, we have also verified that the exact number of galaxy bins does not dominate our results as long as $N_{\rm gal} > N_{\rm GW}$.

As for the last ingredient, we assume cosmic-variance or shot-noise limited uncertainties. In this case, we can write the covariance matrix of the autocorrelation and cross-correlation signals defined in Equations (6.55), (6.59) and (6.61) as the following:

$$\mathrm{Cov}\left[C^{ij}(\ell)C^{mn}(\ell')\right] = \frac{\delta_{\ell\ell'}}{(2\ell+1)f_{\rm sky}} \times \left(\tilde{C}^{im}\tilde{C}^{jn} + \tilde{C}^{in}\tilde{C}^{jm}\right), \tag{6.63}$$

where the indices i, j, m, n can represent both galaxy or gravitational wave bins. The terms $\tilde{C}^{im}$ contain the shot-noise contribution when they represent the autocorrelations in the same bin:

$$\tilde{C}^{im}(\ell) = C^{im}(\ell) + \frac{\delta_{im}}{\bar{n}}, \tag{6.64}$$

where $\bar{n}$ is the average density of projected objects from Equation (6.52). In this work, we assume a survey covering a sky fraction equal to $f_{\rm sky} = 0.5$.

Gaussian Processes

Similarly to what was done in subsection 6.3.2, we try to recover our assumed parameters. The main difference, in this case, is that we focus on the posteriors of $b_{\rm GW}(z)$

and $D_{\rm L,GW}/D_{\rm L,EM}(z)$ according to a Gaussian Process (GP) reconstruction. Our priors in Table 6.2 are imposed both on physical parameters (Ω_m, w_0, H_0) and also on the GP parameters. We consider a certain number of redshift nodes for the two functions, referred to as *training nodes* with a slight abuse of terminology. The amplitudes of the nodes are free and, given a node configuration, we consider GPs which pass through all of these nodes exactly. To render our scenario computationally feasible and not consider many functions for each node configuration, we use the GPs regressor of the `python` package `sklearn` to output the best fit and use this as our function.

Our use of GPs can be thought of as a binning of the functions of interest in redshift space, and imposing a certain prior correlations between the bins. These correlations are specified by the GP kernel function, which in our case is chosen to be

$$\kappa(z_i, z_j;\, L) \propto \exp\left\{-\frac{1}{2}\left(\frac{|z_i - z_j|}{L}\right)^2\right\}, \tag{6.65}$$

where L is the so-called correlation length. This kernel is flexible enough for our purposes, and we do not expect the detailed choice to have any significant impact on our results. For computational purposes, we generate the GPs using a baseline around $D_{\rm L,GW}/D_{\rm L,EM}\,(z) = 1$. This baseline makes the GPs reconstruction to efficiently return to $D_{\rm L,GW}/D_{\rm L,EM}\,(z) = 1$ when not pushed toward other values by the training nodes. For the function $D_{\rm L,GW}/D_{\rm L,EM}(z)$ we also artificially impose the physical constraint $D_{\rm L,GW}/D_{\rm L,EM}(z=0) = 1$ (see Eq. 6.48).

For the setup described in this subsection, we find a total SNR of the GW-gal and GW-GW angular power-spectra of ~ 37. This value is dominated by the GW-gal cross-correlations since the GW-GW autocorrelations are not well measured (SNR$\lesssim 6$). To generalize our choices, in section 6.4.2 we expand on how different combinations of instrumental specifications can affect the precision of the reconstruction.

Results

The results of our Gaussian process reconstruction of the bias $b(z)$ and luminosity distance ratio $D_{\rm L,GW}/D_{\rm L,EM}(z)$ is presented in Figure 6.5. In the same figure, we also compare these constraints to different theoretical models. In the case of the luminosity distance ratio, we use the parametrization

$$\alpha_M(z) = \alpha_0\left[\frac{H_0}{H(z)}\right]^2, \tag{6.66}$$

where we use the Equation (6.45) with $w_0 = -1$ to obtain the plotted lines (Belgacem et al., 2019). On the other hand, for $b_{\rm GW}/b_{\rm gal}\,(z)$ we plot the lines corresponding to constant values of $b_{\rm GW}\,(z)$, while keeping the galaxy bias fixed to the expression in Equation (6.60). As expected, we observe how the fiducial models for both

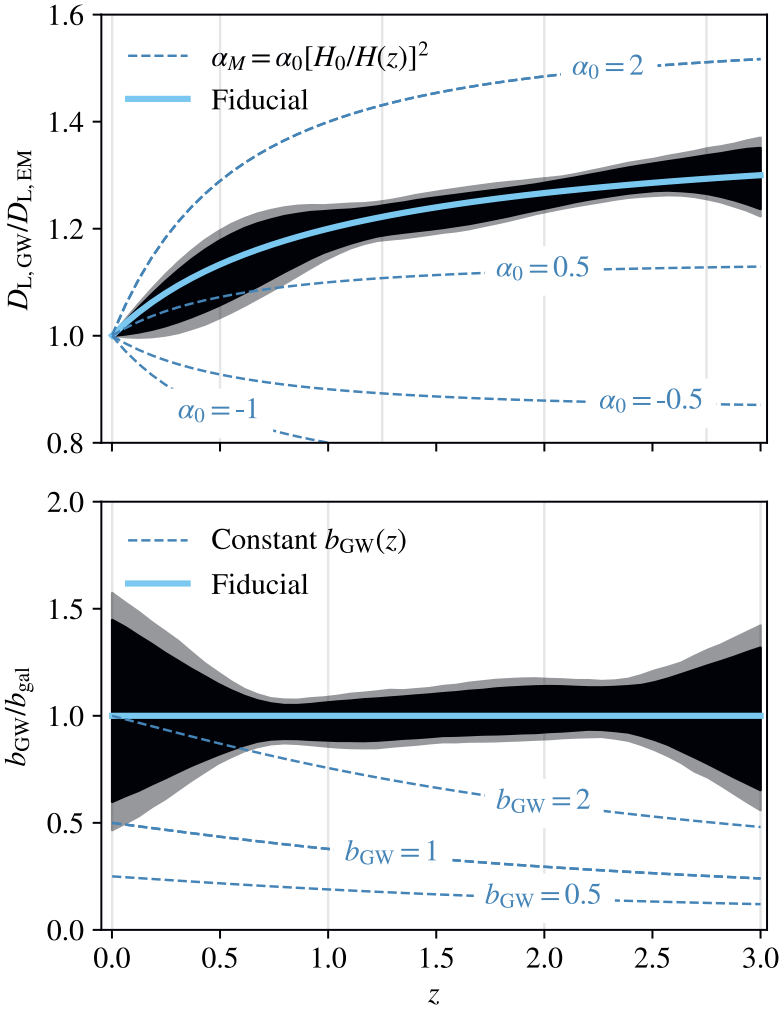

Figure 6.5: Confidence intervals (68%, in black, and 95%, in lighter grey) of the jointly reconstructed functions $D_{\mathrm{L,GW}}/D_{\mathrm{L,EM}}\,(z)$ and $b_{\mathrm{GW}}/b_{\mathrm{gal}}\,(z)$. Together with the assumed fiducial model, we also plot the expectation for different models (see text for more details). The vertical lines mark the fixed location of the nodes used in the GP reconstruction.

$D_{\rm L,GW}/D_{\rm L,EM}\,(z)$ and $b_{\rm GW}/b_{\rm gal}\,(z)$ are well encoded within the reconstructed confidence contours in both panels of Figure 6.5. The constraints at higher redshift ($z \approx 3$) for both reconstructions are broader. This is an effect that could not be seen if a parametric function was used for $D_{\rm L,GW}/D_{\rm L,EM}\,(z)$, for instance, as the parametrization would have fixed the behavior similarly at low and higher redshifts.

In principle, the output of our sampling can also be used to reconstruct the function $\alpha_M(z)$ by calculating the numerical derivative of $D_{\rm L,GW}/D_{\rm L,EM}\,(z)$. For this paper, however, we chose not to do this. The kernel in Equation (6.65) can be interpreted as a smoothness prior, and the value of $\alpha_M(z)$ is directly affected by it. Because of this, if one is interested in inferring $\alpha_M(z)$, GPs should be used to sample this function directly.

The constraining power of our method crucially depends on several observational specifications. The most relevant parameters are (1) the angular sensitivity, specified by the maximum multipole $\ell_{\rm max}$ of the angular power spectra; (2) the number of GW sources, which is specified by the comoving number density $n_{\rm GW}$; and (3) the precision of the GW luminosity distance measurements $\sigma_{\ln D}$. In the case of $n_{\rm GW}$, we adjust the value of n_0 in Equation (6.51) as a way to explore different values of the total number of observed GW events, $N = 4\pi f_{\rm sky}\bar{n}_{\rm GW}$. This, in principle, should include selection effects not captured by our formalism. Obviously, for a given experimental configuration, the mentioned three variables are not independent, but it is still interesting to find the dependence of our results on each one of them separately. This allows us to reach conclusions without relying on specific experiments and to suggest potential design guidelines for future GW detectors.

To attain such insights, in this subsection, we consider constraints on the parametric expression in Equation (6.50), as well as the parametric GW bias given by Equation (6.57). For simplicity, we fix $n = 1$ and only constrain the parameter Ξ_0.

When varying $\ell_{\rm max}$ and N, we keep the rest of the configuration (including the luminosity distance binning) fixed. Each case of $\sigma_{\ln D}$, on the other hand, is accompanied by an adjustment in the number of luminosity distance bins. This is done to be consistent with our binning strategy, namely that the luminosity distance width of each bin is at least $\mathcal{O}(3)$ times wider than $\sigma_{\ln D}$.

Our results are summarized in Figure 6.6, where we plot the anticipated uncertainties in Ξ_0 (upper panel) and b_0 (lower panel) as a function of the SNR of the cross-correlation in Equation (6.61).

For a fixed $\sigma_{\ln D}$, the constraining power on Ξ_0 and b_0 is almost entirely determined by the cross-correlation SNR. This fact suggests that no matter how the given SNR is realized (either by increasing the number of sources or by improving the angular sensitivity), the expected constraints will be the same. This implies that the results presented in this section can be easily scaled to different configurations. Unsurprisingly, we find that the constraints scale as $1/\mathrm{SNR}$.

The situation is somewhat different for the case of varying $\sigma_{\ln D}$ (and the number of

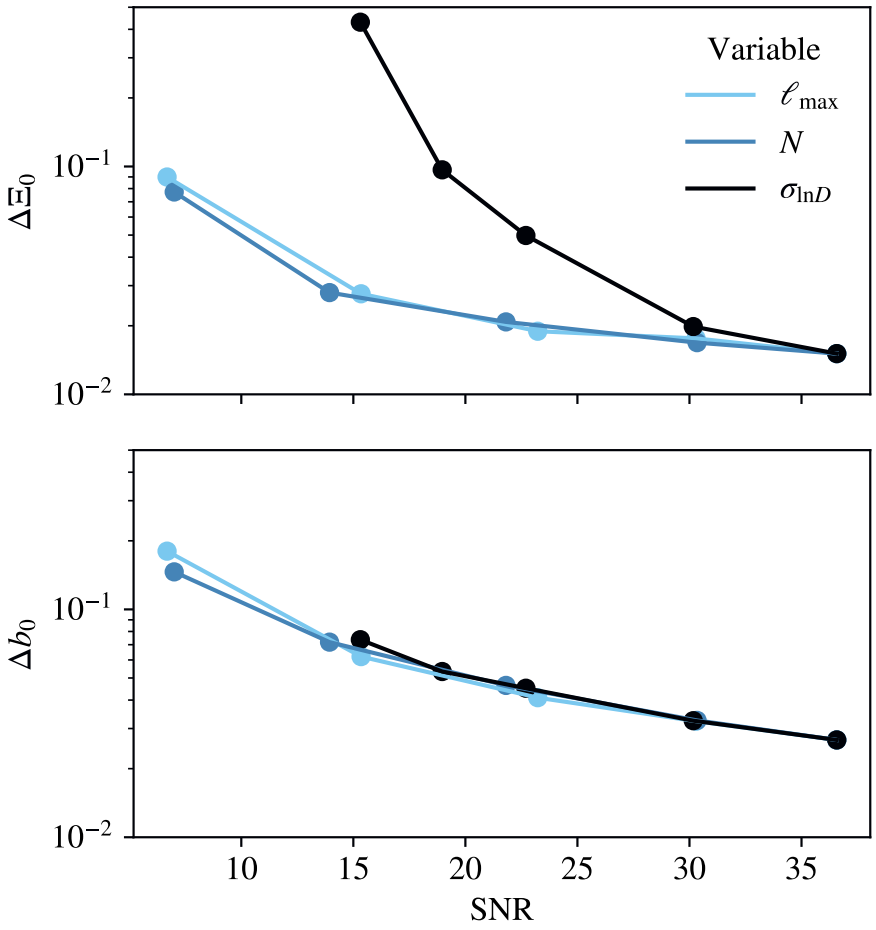

Figure 6.6: Scaling of the observed constraints with the cross-correlation SNR. Using a parametrized model for $b_{\rm GW}/b_{\rm gal}\,(z)$ and $D_{\rm L,GW}/D_{\rm L,EM}\,(z)$ we explore the constraining power of our method as a function of the number of observed GW sources $N = [0.7, 4, 7, 13, 20] \times 10^4$, angular resolution $\ell_{\rm max} = [20, 40, 60, 80, 100]$ and luminosity distance uncertainty $\sigma_{\ln D} = [0.5, 0.3, 0.2, 0.075, 0.05]$. As visible from the figure, the data SNR completely captures the effect on the observed uncertainties Δb_0 and $\Delta\Xi_0$ in the first two cases. In the case of $\sigma_{\ln D}$, we observe that the increase in constraining power for $D_{\rm L,GW}/D_{\rm L,EM}\,(z)$ is steeper due to the larger number of window functions that we can build to sample $D_{\rm L,GW}\,(z)$.

luminosity distance bins). The constraints on the bias still follow the same form (see the lower panel), but the scaling of the Ξ_0 constraints, on the other hand, is much steeper than in the cases of varying $\ell_{\rm max}$ and $n_{\rm GW}$, roughly $1/{\rm SNR}^3$. This fact can be qualitatively understood by remembering the importance of the relative positions of GW and galaxy window functions demonstrated in Figure 6.4. Sampling this relation with a higher number of window functions increases the precision of our reconstruction.

The results presented in this section quantify the importance of accurate luminosity distance measurements and demonstrate the benefit that smaller values of $\sigma_{\ln D}$ can bring to a binned approach.

6.4.3 Comparison with previous works

Our formalism, based on binned angular power-spectra and sky maps, is optimal for many sources with no known counterpart. Its main advantages are related to the simple modeling of the theoretical signals and their data covariance matrix. Because no reconstruction of the underlying density field is necessary, the predictions display a clear separation of scales. For example, the angular scales that we have considered hare are all within the linear regime ($k \lesssim 0.1$ Mpc^{-1}). Furthermore, because this formalism is well established, our shot-noise limited covariance matrix can be easily generalized to include additional sources of (co-)variance.

Although a comprehensive comparison between multiple approaches is outside the scope of this work, it is worth discussing how our results compare to others found in the literature. However, we preface this by saying that one-to-one comparisons are often complicated either by significantly different assumptions or the impossibility of directly translating these assumptions from one prescription to another. Despite this, here, we draw a parallel between our method and two other methods.

The first method is the one used in Mukherjee et al. (2020), which has also been shown to be extremely successful in measuring both $b_{\rm GW}(z)$ and $D_{\rm L,GW}(z)$ using parametric models. Similarly to this work, the information is also extracted from the cross-correlation with redshift sources, but no binning of the GW data is performed. In this case, we have verified that such methods perform significantly better than our map-based approach in the case of a low number density of GW sources and large uncertainty in the measured $D_{\rm L,EM}(z)$. These features, in particular, make it especially useful for near-future samples of a few tens of objects.

The second promising method to measure $D_{\rm L,GW}(z)$ proposed in the literature is offered by GW sources with known counterparts. Such observations give direct access to $D_{\rm L,GW}$ as a function of redshift and can be combined with similar measurements in the EM spectrum to obtain $D_{\rm L,GW}/D_{\rm L,EM}(z)$. The analysis of Belgacem et al. (2020) is based on this methodology and, similarly to ours, also employs GPs to reconstruct this ratio from an Einstein Telescope sample with $\sim 10^2$ sources. Ultimately, we expect this counterpart-based formalism and the one described in this work to be complementary:

a direct measure of $D_{\mathrm{L,GW}}(z)$ can be used to break the degeneracy between the bias and luminosity distance reconstruction. However, we do not attempt to combine the two methods here because the fraction of events with known counterparts that will be observed is heavily dependent on both the GW source distribution and multiple instrumental setups.

6.5 Conclusions

In Section 6.2 we have explored the impact of gravitational lensing on the soon to be measured merger rates of GW mergers. These results offer guidance when interpreting magnification effects and are intentionally agnostic regarding detector or source population. The main result is that the presence of a lensed population in an observed sample is easily recognizable. This conclusion hinges only on the weak dependence of the inferred binary properties on the factor μ and provides a general explanation for the established result that lensing contamination for luminosity-limited GW events are low for a wide range of detectors and source populations (e.g. Sereno et al., 2010; Ding et al., 2015; Ng et al., 2018; Oguri, 2018).

In Section 6.3 we have quantified for the first time the need for high-resolution GW detectors to extract the total information content of the GWB of astrophysical origin. In particular, we have shown that both a high angular resolution and a high signal-to-noise ratio ($\ell \sim 100$, S/N ~ 70) are required to recover both the matter abundance Ω_{m} and features of the kernel $\mathcal{K}(r)$ as a function of redshift. Note, in particular, that these requirements exceed the angular resolution of present-day and near-future detectors (roughly $\ell \lesssim 10$, and even $\ell \lesssim 4$ for LISA (Ungarelli and Vecchio, 2001; LIGO Scientific collaboration and VIRGO collaboration, 2019)). While this is not the priority of currently proposed third-generation detectors (Maggiore et al., 2020a), it is worth noting that the advantages of high-resolution gravitational-wave astronomy are numerous and not limited to the study of this anisotropic background (Baker et al., 2019). Furthermore, the case for studying the cross-correlation is strengthened by noticing that the anisotropies of the GWB in the kHz band will most probably first be measured through cross-correlation with galaxy surveys. The galaxy map provides a guiding pattern look into the noisy GW data and therefore enhances the SNR.

Finally, the work presented in Section 6.4 shows that the combination of GW resolved events and the clustering of galaxies is expected to improve our current knowledge of the physics of GW mergers and GW propagation. We have discussed how to reconstruct these properties as a function of redshift in a generic way and highlighted the need for accurate and precise measurements of $D_{\mathrm{L,GW}}$. This will require control over the instrument calibration uncertainties (Cahillane et al., 2017), but also the degeneracy between the inclination of the source and its luminosity distance (Ghosh et al., 2016). In the future, we aim to apply our current analysis pipeline to the next generation of large-scale structure surveys and incoming GW observations.

Given the promising nature of our results, we believe that the cross-correlation between GW and galaxy catalogs has the potential to be a robust observational probe in the era of multimessenger cosmology.

Appendices

6A Shot-noise for the background cross-correlation signal

We follow (Jenkins, Alexander C. and Sakellariadou, Mairi, 2019) and evaluate the shot-noise contribution to the observed cross-correlation signal $C_\ell^\times$ in terms of the shot-noise contribution to the covariance between the observed maps $\Omega(\hat{\mathbf{r}})$ and $\Delta(\hat{\mathbf{r}}')$. Our starting point is

$$B_\ell = \int d^2\hat{\mathbf{r}} P_\ell(\hat{\mathbf{r}}\cdot\hat{\mathbf{r}}')\mathrm{Cov}[\Omega(\hat{\mathbf{r}}),\Delta(\hat{\mathbf{r}}')]_{\mathrm{SN}}. \tag{6.67}$$

By keeping in mind that $\tilde{\mathcal{K}}(r) = r^2\mathcal{K}(r)\bar{n}(r)$ and that $\delta_g(\vec{\mathbf{r}}) = \left(n(\vec{\mathbf{r}}) - \bar{n}(r)\right)/\bar{n}$ we use the definitions in Eqs. (6.22), (6.32) to write:

$$\mathrm{Cov}[\Omega(\hat{\mathbf{r}}),\Delta(\hat{\mathbf{r}}')]_{\mathrm{SN}} = \int dr \int dr' \frac{r^2}{\bar{n}} \times \mathrm{Cov}[\mathcal{K}(r)n(\vec{\mathbf{r}}), W_i(r')n(\vec{\mathbf{r}}')]_{\mathrm{SN}}. \tag{6.68}$$

As a side note, we point out that this expression is a stretch of notation since, formally, the quantities $\mathcal{K}(r)n(\vec{\mathbf{r}})$ and $W(r)n(\vec{\mathbf{r}})$ represent the mean values of the variables that we are trying to correlate. To proceed, we notice that $W(r)n(\vec{\mathbf{r}})$ is proportional to the number density of galaxies visible in the galaxy survey and that $\mathcal{K}(r)n(\vec{\mathbf{r}})$ is proportional to the number density of GW events around an infinitesimal volume centered in $\vec{\mathbf{r}}$. This is confirmed by the formalism used in the references mentioned above, (Jenkins, Alexander C. and Sakellariadou, Mairi, 2019) and (Cusin et al., 2018), to predict a realistic $\mathcal{K}(r)$.

In a finite volume δV_i we write down the number of GW mergers as

$$\Lambda_i = \sum_k^{N_i} \lambda_k, \tag{6.69}$$

where N is the number of galaxies present in this volume and the λ_j-s are the number of events for each galaxy. If we assume that N and λ_k are Poisson distributed, Λ_i follows a compound Poisson distribution with variance

$$\mathrm{Var}[\Lambda_i] = \langle\Lambda_i^2\rangle - \langle\Lambda_i\rangle^2 = \langle N_i\rangle\left(\langle\lambda\rangle + \langle\lambda\rangle^2\right). \tag{6.70}$$

If we call f the fraction of galaxies in the volume δV_j visible in the galaxy survey we also derive:

$$\mathrm{Cov}[fN_j, \Lambda_i] = f\langle N\rangle\langle\lambda\rangle\delta_{ij}, \tag{6.71}$$

where δ_{ij} is the Kronecker delta. By going back to the continuous case, we obtain the following result:

$$\mathrm{Cov}[\mathcal{K}(r)n(\vec{\mathbf{r}}), W_i(r')n(\vec{\mathbf{r}}')]_{\rm SN} = \bar{n}(r)W_i(r)\mathcal{K}(r)\delta^3(\vec{\mathbf{r}} - \vec{\mathbf{r}}'). \tag{6.72}$$

Finally, by plugging everything into Eq. (6.67), we obtain the result shown in the main text:

$$B_\ell = \int dr\; W_i(r)\mathcal{K}(r). \tag{6.73}$$

6B Cosmic variance of the background cross-correlation signal

Assume we have two maps on the sky, corresponding to the GWB and GC anisotropies. The angular decomposition coefficients $a_{\ell m}^{\rm GW}$ and $a_{\ell m}^{\rm GC}$ are assumed to be Gaussian random variables with zero mean, and each m-mode is drawn from the same distribution. The relevant angular power spectra are defined as

$$C_\ell^\times \equiv \mathrm{Cov}\left[a_{\ell m}^{\rm GW}, a_{\ell m}^{\rm GC}\right], \quad C_\ell^{\rm GW} \equiv \mathrm{Var}\left[a_{\ell m}^{\rm GW}\right], \quad C_\ell^{\rm GC} \equiv \mathrm{Var}\left[a_{\ell m}^{\rm GC}\right]. \tag{6.74}$$

It is then trivial to construct an unbiased estimator of the cross-correlation power spectrum as

$$\widehat{C_\ell^\times} = \frac{1}{2\ell+1}\sum_{m=-\ell}^{+\ell} a_{\ell m}^{\rm GW} a_{\ell m}^{\rm GC}. \tag{6.75}$$

The variance of this estimator can then be shown to be

$$\begin{aligned}\mathrm{Var}C_\ell^\times =& \frac{1}{(2\ell+1)^2}\sum_{m=-\ell}^{+\ell}\mathrm{Var}\left[a_{\ell m}^{\rm GW}a_{\ell m}^{\rm GC}\right] = \frac{1}{(2\ell+1)^2}\sum_{m=-\ell}^{+\ell} C_\ell^{\rm GW}C_\ell^{\rm GC} + \\ & \mathrm{Cov}\left[\left(a_{\ell m}^{\rm GW}\right)^2, \left(a_{\ell m}^{\rm GC}\right)^2\right] - \mathrm{Cov}\left[a_{\ell m}^{\rm GW}, a_{\ell m}^{\rm GC}\right]^2.\end{aligned} \tag{6.76}$$

In summary, we have

$$\mathrm{Var}C_\ell^\times = \frac{C_\ell^{\rm GW}C_\ell^{\rm GC} + \left(C_\ell^\times\right)^2}{2\ell+1}, \tag{6.77}$$

where we have used the Gaussianity of $a_{\ell m}$'s. Making the $a_{\ell m}^{\rm GC} \to a_{\ell m}^{\rm GW}$ replacement turns this expression into

$$\mathrm{Var} C_\ell^{\rm GW} = \frac{2\left(C_\ell^{\rm GW}\right)^2}{2\ell+1}, \tag{6.78}$$

which, of course, recovers the usual cosmic variance result.

Bibliography

B. P. Abbott, R. Abbott, T. D. Abbott, S. Abraham, F. Acernese, K. Ackley, C. Adams, R. X. Adhikari, V.B. Adya, C. Affeldt, and et al. Gwtc-1: A gravitational-wave transient catalog of compact binary mergers observed by ligo and virgo during the first and second observing runs. *Physical Review X*, 9(3), Sep 2019. ISSN 2160-3308. doi: 10.1103/physrevx.9.031040.

B. P. Abbott et al. Astrophysical Implications of the Binary Black-hole Merger GW150914. ApJ, 818:L22, February 2016. doi: 10.3847/2041-8205/818/2/L22.

B. P. Abbott et al. Observation of Gravitational Waves from a Binary Black Hole Merger. *Phys. Rev. Lett.*, 116(6):061102, 2016. doi: 10.1103/PhysRevLett.116.061102.

R. Abbott, T. D. Abbott, S. Abraham, F. Acernese, K. Ackley, A. Adams, C. Adams, R. X. Adhikari, V. B. Adya, C. Affeldt, and et al. Population Properties of Compact Objects from the Second LIGO-Virgo Gravitational-Wave Transient Catalog. 10 2020.

N. Aghanim et al. Planck 2018 results. I. Overview and the cosmological legacy of Planck. *Astron. Astrophys.*, 641:A1, 2020. doi: 10.1051/0004-6361/201833880.

Luca Amendola, Ignacy Sawicki, Martin Kunz, and Ippocratis D. Saltas. Direct detection of gravitational waves can measure the time variation of the planck mass. *Journal of Cosmology and Astroparticle Physics*, 2018(08):030–030, Aug 2018. ISSN 1475-7516. doi: 10.1088/1475-7516/2018/08/030.

Shin'ichiro Ando, Aurélien Benoit-Lévy, and Eiichiro Komatsu. Mapping dark matter in the gamma-ray sky with galaxy catalogs. Phys. Rev. D, 90(2):023514, July 2014. doi: 10.1103/PhysRevD.90.023514.

Shun Arai and Atsushi Nishizawa. Generalized framework for testing gravity with gravitational-wave propagation. II. Constraints on Horndeski theory. Phys. Rev. D, 97(10):104038, May 2018. doi: 10.1103/PhysRevD.97.104038.

John Baker et al. High angular resolution gravitational wave astronomy. 8 2019.

Tessa Baker and Ian Harrison. Constraining Scalar-Tensor Modified Gravity with Gravitational Waves and Large Scale Structure Surveys. *JCAP*, 01:068, 2021. doi: 10.1088/1475-7516/2021/01/068.

Krzysztof Belczynski, Daniel E. Holz, Tomasz Bulik, and Richard O'Shaughnessy. The first gravitational-wave source from the isolated evolution of two stars in the 40-100 solar mass range. Nature, 534(7608):512–515, Jun 2016. doi: 10.1038/nature18322.

Krzysztof Belczynski, Taeho Ryu, Rosalba Perna, Emanuele Berti, Takamitsu L. Tanaka, and Tomasz Bulik. On the likelihood of detecting gravitational waves from Population III compact object binaries. MNRAS, 471(4):4702–4721, Nov 2017. doi: 10.1093/mnras/stx1759.

Enis Belgacem, Yves Dirian, Stefano Foffa, and Michele Maggiore. Modified gravitational-wave propagation and standard sirens. *Phys. Rev. D*, 98(2):023510, 2018. doi: 10.1103/PhysRevD.98.023510.

Enis Belgacem, Stefano Foffa, Michele Maggiore, and Tao Yang. Gaussian processes reconstruction of modified gravitational wave propagation. *Phys. Rev. D*, 101(6):063505, 2020. doi: 10.1103/PhysRevD.101.063505.

Enis Belgacem et al. Testing modified gravity at cosmological distances with LISA standard sirens. *JCAP*, 07:024, 2019. doi: 10.1088/1475-7516/2019/07/024.

Emilio Bellini and Ignacy Sawicki. Maximal freedom at minimum cost: linear large-scale structure in general modifications of gravity. *JCAP*, 07:050, 2014. doi: 10.1088/1475-7516/2014/07/050.

Sayantani Bera, Divya Rana, Surhud More, and Sukanta Bose. Incompleteness Matters Not: Inference of H_0 from Binary Black Hole–Galaxy Cross-correlations. *Astrophys. J.*, 902(1):79, 2020. doi: 10.3847/1538-4357/abb4e0.

Daniele Bertacca, Angelo Ricciardone, Nicola Bellomo, Alexander C. Jenkins, Sabino Matarrese, Alvise Raccanelli, Tania Regimbau, and Mairi Sakellariadou. Projection effects on the observed angular spectrum of the astrophysical stochastic gravitational wave background. *arXiv e-prints*, art. arXiv:1909.11627, September 2019.

B. Bertotti, L. Iess, and P. Tortora. A test of general relativity using radio links with the Cassini spacecraft. Nature, 425(6956):374–376, September 2003. doi: 10.1038/nature01997.

Simeon Bird, Ilias Cholis, Julian B. Muñoz, Yacine Ali-Haïmoud, Marc Kamionkowski, Ely D. Kovetz, Alvise Raccanelli, and Adam G. Riess. Did LIGO detect dark matter? *Phys. Rev. Lett.*, 116(20):201301, 2016. doi: 10.1103/PhysRevLett.116.201301.

Luc Blanchet, Thibault Damour, Bala R. Iyer, Clifford M. Will, and Alan G. Wiseman. Gravitational-Radiation Damping of Compact Binary Systems to Second Post-Newtonian Order. Phys. Rev. Lett., 74(18):3515–3518, May 1995. doi: 10.1103/PhysRevLett.74.3515.

Tom Broadhurst, Jose M. Diego, and III Smoot, George. Reinterpreting Low Frequency LIGO/Virgo Events as Magnified Stellar-Mass Black Holes at Cosmological Distances. *arXiv e-prints*, art. arXiv:1802.05273, Feb 2018.

Tom Broadhurst, Jose M. Diego, and III Smoot, George F. Twin LIGO/Virgo Detections of a Viable Gravitationally-Lensed Black Hole Merger. *arXiv e-prints*, art. arXiv:1901.03190, Jan 2019.

Craig Cahillane, Joe Betzwieser, Duncan A. Brown, Evan Goetz, Evan D. Hall, Kiwamu Izumi, Shivaraj Kandhasamy, Sudarshan Karki, Jeff S. Kissel, Greg Mendell, Richard L. Savage, Darkhan Tuyenbayev, Alex Urban, Aaron Viets, Madeline Wade, and Alan J. Weinstein. Calibration uncertainty for Advanced LIGO's first and second observing runs. Phys. Rev. D, 96(10):102001, November 2017. doi: 10.1103/PhysRevD.96.102001.

Gianluca Calcagni, Sachiko Kuroyanagi, Sylvain Marsat, Mairi Sakellariadou, Nicola Tamanini, and Gianmassimo Tasinato. Quantum gravity and gravitational-wave astronomy. *JCAP*, 10:012, 2019. doi: 10.1088/1475-7516/2019/10/012.

Giulia Cusin, Cyril Pitrou, and Jean-Philippe Uzan. Anisotropy of the astrophysical gravitational wave background: Analytic expression of the angular power spectrum and correlation with cosmological observations. Phys. Rev. D, 96(10):103019, Nov 2017. doi: 10.1103/PhysRevD.96.103019.

Giulia Cusin, Irina Dvorkin, Cyril Pitrou, and Jean-Philippe Uzan. First Predictions of the Angular Power Spectrum of the Astrophysical Gravitational Wave Background. Phys. Rev. Lett., 120(23):231101, Jun 2018. doi: 10.1103/PhysRevLett.120.231101.

Giulia Cusin, Irina Dvorkin, Cyril Pitrou, and Jean-Philippe Uzan. Comment on the article "Anisotropies in the astrophysical gravitational-wave background: The impact of black hole distributions" by A.C. Jenkins et al. [arXiv:1810.13435]. 2018.

Giulia Cusin, Irina Dvorkin, Cyril Pitrou, and Jean-Philippe Uzan. Properties of the stochastic astrophysical gravitational wave background: astrophysical sources dependencies. 2019.

Liang Dai, Tejaswi Venumadhav, and Kris Sigurdson. Effect of lensing magnification on the apparent distribution of black hole mergers. Phys. Rev. D, 95(4):044011, Feb 2017. doi: 10.1103/PhysRevD.95.044011.

Benedikt Diemer. COLOSSUS: A python toolkit for cosmology, large-scale structure, and dark matter halos. *Astrophys. J. Suppl.*, 239(2):35, 2018. doi: 10.3847/1538-4365/aaee8c.

Xuheng Ding, Marek Biesiada, and Zong-Hong Zhu. Strongly lensed gravitational waves from intrinsically faint double compact binaries—prediction for the Einstein Telescope. *Journal of Cosmology and Astro-Particle Physics*, 2015(12):006, Dec 2015. doi: 10.1088/1475-7516/2015/12/006.

Yves Dirian, Stefano Foffa, Martin Kunz, Michele Maggiore, and Valeria Pettorino. Non-local gravity and comparison with observational datasets. ii. updated results and bayesian model comparison with λcdm. *Journal of Cosmology and Astroparticle Physics*, 2016(05):068–068, May 2016. ISSN 1475-7516. doi: 10.1088/1475-7516/2016/05/068.

Michal Dominik, Krzysztof Belczynski, Christopher Fryer, Daniel E. Holz, Emanuele Berti, Tomasz Bulik, Ilya Mand el, and Richard O'Shaughnessy. Double Compact Objects. I. The Significance of the Common Envelope on Merger Rates. ApJ, 759(1):52, Nov 2012. doi: 10.1088/0004-637X/759/1/52.

Michal Dominik, Krzysztof Belczynski, Christopher Fryer, Daniel E. Holz, Emanuele Berti, Tomasz Bulik, Ilya Mandel, and Richard O'Shaughnessy. Double Compact Objects. II. Cosmological Merger Rates. ApJ, 779(1):72, Dec 2013. doi: 10.1088/0004-637X/779/1/72.

Albert Einstein. Näherungsweise Integration der Feldgleichungen der Gravitation. *Sitzungsberichte der Königlich Preußischen Akademie der Wissenschaften (Berlin*, pages 688–696, Jan 1916.

Albert Einstein. Über Gravitationswellen. *Sitzungsberichte der Königlich Preußischen Akademie der Wissenschaften (Berlin), Seite 154-167.*, 1918.

Daniel Foreman-Mackey, David W. Hogg, Dustin Lang, and Jonathan Goodman. emcee: The MCMC Hammer. *Publ. Astron. Soc. Pac.*, 125:306–312, 2013. doi: 10.1086/670067.

Archisman Ghosh, Walter Del Pozzo, and Parameswaran Ajith. Estimating parameters of binary black holes from gravitational-wave observations of their inspiral, merger and ringdown. *Phys. Rev. D*, 94(10):104070, 2016. doi: 10.1103/PhysRevD.94.104070.

R. Hada and T. Futamase. Forecasts of cosmological constraints from Type Ia supernovae including the weak-lensing convergence. *arXiv e-prints*, October 2018.

Evan D. Hall and Matthew Evans. Metrics for next-generation gravitational-wave detectors. *Classical and Quantum Gravity*, 36(22):225002, November 2019. doi: 10.1088/1361-6382/ab41d6.

O. A. Hannuksela, K. Haris, K. K. Y. Ng, S. Kumar, A. K. Mehta, D. Keitel, T. G. F. Li, and P. Ajith. Search for Gravitational Lensing Signatures in LIGO-Virgo Binary Black Hole Events. ApJ, 874(1):L2, Mar 2019. doi: 10.3847/2041-8213/ab0c0f.

Stefan Hilbert, Simon D. M. White, Jan Hartlap, and Peter Schneider. Strong lensing optical depths in a ΛCDM universe. MNRAS, 382(1):121–132, Nov 2007. doi: 10.1111/j.1365-2966.2007.12391.x.

Daniel E. Holz and Eric V. Linder. Safety in numbers: Gravitational lensing degradation of the luminosity distance–redshift relation. *The Astrophysical Journal*, 631(2):678–688, oct 2005. doi: 10.1086/432085.

Gregory Walter Horndeski. Second-order scalar-tensor field equations in a four-dimensional space. *Int. J. Theor. Phys.*, 10:363–384, 1974. doi: 10.1007/BF01807638.

Bin Hu, Marco Raveri, Noemi Frusciante, and Alessandra Silvestri. Effective Field Theory of Cosmic Acceleration: an implementation in CAMB. *Phys. Rev.*, D89(10):103530, 2014. doi: 10.1103/PhysRevD.89.103530.

Alexander C. Jenkins, Mairi Sakellariadou, Tania Regimbau, and Eric Slezak. Anisotropies in the astrophysical gravitational-wave background: Predictions for the detection of compact binaries by LIGO and Virgo. *Phys. Rev.*, D98(6):063501, 2018. doi: 10.1103/PhysRevD.98.063501.

Alexander C. Jenkins, Joseph D. Romano, and Mairi Sakellariadou. Estimating the angular power spectrum of the gravitational-wave background in the presence of shot noise. 2019a.

Alexander C. Jenkins, Mairi Sakellariadou, Tania Regimbau, Eric Slezak, Richard O'Shaughnessy, and Daniel Wysocki. Response to Cusin et al's comment on arXiv:1810.13435. 2019b.

Jenkins, Alexander C. and Sakellariadou, Mairi. Anisotropies in the stochastic gravitational-wave background: Formalism and the cosmic string case. *Phys. Rev.*, D98(6):063509, 2018. doi: 10.1103/PhysRevD.98.063509.

Jenkins, Alexander C. and Sakellariadou, Mairi. Shot noise in the astrophysical gravitational-wave background. 2019.

Bence Kocsis, Zsolt Frei, Zoltan Haiman, and Kristen Menou. Finding the electromagnetic counterparts of cosmological standard sirens. *The Astrophysical Journal*, 637(1):27–37, jan 2006. doi: 10.1086/498236.

Macarena Lagos, Maya Fishbach, Philippe Landry, and Daniel E. Holz. Standard sirens with a running Planck mass. Phys. Rev. D, 99(8):083504, April 2019. doi: 10.1103/PhysRevD.99.083504.

Antony Lewis. GetDist: a Python package for analysing Monte Carlo samples. 2019.

LIGO Scientific collaboration and VIRGO collaboration. Directional limits on persistent gravitational waves using data from Advanced LIGO's first two observing runs. Phys. Rev. D, 100(6):062001, September 2019. doi: 10.1103/PhysRevD.100.062001.

P. Madau, L. Pozzetti, and M. Dickinson. The Star Formation History of Field Galaxies. ApJ, 498:106–116, May 1998. doi: 10.1086/305523.

Michele Maggiore, Chris Van Den Broeck, Nicola Bartolo, Enis Belgacem, Daniele Bertacca, Marie Anne Bizouard, Marica Branchesi, Sebastien Clesse, Stefano Foffa, Juan García-Bellido, Stefan Grimm, Jan Harms, Tanja Hinderer, Sabino Matarrese, Cristiano Palomba, Marco Peloso, Angelo Ricciardone, and Mairi Sakellariadou. Science case for the einstein telescope. *Journal of Cosmology and Astroparticle Physics*, 2020(03):050–050, mar 2020a. doi: 10.1088/1475-7516/2020/03/050. URL https://doi.org/10.1088%2F1475-7516%2F2020%2F03%2F050.

Michele Maggiore et al. Science Case for the Einstein Telescope. *JCAP*, 03:050, 2020b. doi: 10.1088/1475-7516/2020/03/050.

Jose María Ezquiaga. Hearing gravity from the cosmos: GWTC-2 probes general relativity at cosmological scales. *arXiv e-prints*, art. arXiv:2104.05139, April 2021.

D. V. Martynov, E. D. Hall, B. P. Abbott, R. Abbott, T. D. Abbott, C. Adams, R. X. Adhikari, R. A. Anderson, S. B. Anderson, K. Arai, and et al. Sensitivity of the Advanced LIGO detectors at the beginning of gravitational wave astronomy. Phys. Rev. D, 93 (11):112004, Jun 2016. doi: 10.1103/PhysRevD.93.112004.

Suvodip Mukherjee, Benjamin D. Wandelt, and Joseph Silk. Testing the general theory of relativity using gravitational wave propagation from dark standard sirens. 12 2020. doi: 10.1093/mnras/stab001.

Mattia Negrello, R. Hopwood, G. De Zotti, and et al. The Detection of a Population of Submillimeter-Bright, Strongly Lensed Galaxies. *Science*, 330(6005):800, Nov 2010. doi: 10.1126/science.1193420.

K. K. Y. Ng, K. W. K. Wong, T. Broadhurst, and T. G. F. Li. Precise LIGO lensing rate predictions for binary black holes. Phys. Rev. D, 97(2):023012, January 2018. doi: 10.1103/PhysRevD.97.023012.

Masamune Oguri. Measuring the distance-redshift relation with the cross-correlation of gravitational wave standard sirens and galaxies. Phys. Rev. D, 93(8):083511, Apr 2016. doi: 10.1103/PhysRevD.93.083511.

Masamune Oguri. Measuring the distance-redshift relation with the cross-correlation of gravitational wave standard sirens and galaxies. *Phys. Rev. D*, 93(8):083511, 2016. doi: 10.1103/PhysRevD.93.083511.

Masamune Oguri. Effect of gravitational lensing on the distribution of gravitational waves from distant binary black hole mergers. MNRAS, 480(3):3842–3855, Nov 2018. doi: 10.1093/mnras/sty2145.

A. M. Price-Whelan et al. The Astropy Project: Building an Open-science Project and Status of the v2.0 Core Package. *Astron. J.*, 156(3):123, 2018. doi: 10.3847/1538-3881/aabc4f.

Alvise Raccanelli, Ely D. Kovetz, Simeon Bird, Ilias Cholis, and Julian B. Munoz. Determining the progenitors of merging black-hole binaries. *Phys. Rev. D*, 94(2):023516, 2016. doi: 10.1103/PhysRevD.94.023516.

Carl Edward Rasmussen and Christopher K. I. Williams. *Gaussian Processes for Machine Learning (Adaptive Computation and Machine Learning)*. The MIT Press, 2005. ISBN 026218253X.

Marco Raveri, Bin Hu, Noemi Frusciante, and Alessandra Silvestri. Effective Field Theory of Cosmic Acceleration: constraining dark energy with CMB data. *Phys. Rev.*, D90(4):043513, 2014. doi: 10.1103/PhysRevD.90.043513.

Thomas P. Robitaille et al. Astropy: A Community Python Package for Astronomy. *Astron. Astrophys.*, 558:A33, 2013. doi: 10.1051/0004-6361/201322068.

B. S. Sathyaprakash, B. F. Schutz, and C. Van Den Broeck. Cosmography with the Einstein Telescope. *Classical and Quantum Gravity*, 27(21):215006, Nov 2010. doi: 10.1088/0264-9381/27/21/215006.

Giulio Scelfo, Nicola Bellomo, Alvise Raccanelli, Sabino Matarrese, and Licia Verde. GW\times$LSS: chasing the progenitors of merging binary black holes. *JCAP*, 09: 039, 2018a. doi: 10.1088/1475-7516/2018/09/039.

Giulio Scelfo, Nicola Bellomo, Alvise Raccanelli, Sabino Matarrese, and Licia Verde. Gwxlss: chasing the progenitors of merging binary black holes. *Journal of Cosmology and Astroparticle Physics*, 2018(09):039–039, sep 2018b. doi: 10.1088/1475-7516/2018/09/039.

Giulio Scelfo, Lumen Boco, Andrea Lapi, and Matteo Viel. Exploring galaxies-gravitational waves cross-correlations as an astrophysical probe. *JCAP*, 10:045, 2020. doi: 10.1088/1475-7516/2020/10/045.

Joop Schaye et al. The EAGLE project: Simulating the evolution and assembly of galaxies and their environments. *Mon. Not. Roy. Astron. Soc.*, 446:521–554, 2015. doi: 10.1093/mnras/stu2058.

P. Schechter. An analytic expression for the luminosity function for galaxies. ApJ, 203: 297–306, January 1976. doi: 10.1086/154079.

Bernard F. Schutz. Determining the Hubble Constant from Gravitational Wave Observations. *Nature*, 323:310–311, 1986. doi: 10.1038/323310a0.

Scikit-learn. Scikit-learn 0.19.1 documentation: Gaussian Processes. http://scikit-learn.org/stable/modules/gaussian_process.html, 2018. Accessed: 10-06-2019.

M. Sereno, A. Sesana, A. Bleuler, P. Jetzer, M. Volonteri, and M. C. Begelman. Strong Lensing of Gravitational Waves as Seen by LISA. *Physical Review Letters*, 105(25): 251101, December 2010. doi: 10.1103/PhysRevLett.105.251101.

L. P. Singer, D. A. Goldstein, and J. S. Bloom. The Two LIGO/Virgo Binary Black Hole Mergers on 2019 August 28 Were Not Strongly Lensed. *arXiv e-prints*, October 2019.

Graham P. Smith, Mathilde Jauzac, John Veitch, Will M. Farr, Richard Massey, and Johan Richard. What if LIGO's gravitational wave detections are strongly lensed by massive galaxy clusters? MNRAS, 475(3):3823–3828, Apr 2018. doi: 10.1093/mnras/sty031.

R. Takahashi, M. Oguri, M. Sato, and T. Hamana. Probability Distribution Functions of Cosmological Lensing: Convergence, Shear, and Magnification. ApJ, 742:15, November 2011. doi: 10.1088/0004-637X/742/1/15.

A. Taruya, M. Takada, T. Hamana, I. Kayo, and T. Futamase. Lognormal Property of Weak-Lensing Fields. ApJ, 571:638–653, June 2002. doi: 10.1086/340048.

Eric Thrane, Stefan Ballmer, Joseph D. Romano, Sanjit Mitra, Dipongkar Talukder, Sukanta Bose, and Vuk Mand ic. Probing the anisotropies of a stochastic gravitational-wave background using a network of ground-based laser interferometers. Phys. Rev. D, 80(12):122002, December 2009. doi: 10.1103/PhysRevD.80.122002.

Carlo Ungarelli and Alberto Vecchio. Studying the anisotropy of the gravitational wave stochastic background with lisa. *Phys. Rev. D*, 64:121501, Nov 2001. doi: 10.1103/PhysRevD.64.121501. URL https://link.aps.org/doi/10.1103/PhysRevD.64.121501.

A. Weltman et al. Fundamental physics with the Square Kilometre Array. *Publ. Astron. Soc. Austral.*, 37:e002, 2020. doi: 10.1017/pasa.2019.42.

J. S. B. Wyithe and A. Loeb. Magnification of light from many distant quasars by gravitational lenses. Nature, 417:923–925, June 2002. doi: 10.1038/nature00794.